Biochemical, biophysical, and structural investigations of two mutants (C154Y and R312H) of the human Kir2.1 channel involved in the Andersen-Tawil syndrome

Dania Zuniga, Andreas Zoumpoulakis, Rafael Veloso, Laurie Peverini, Sophie Shi, Alexandre Pozza, Valérie Kugler, Françoise Bonneté, Tahar Bouceba, Renaud Wagner, et al.

Biochemical, biophysical, and structural investigations of two mutants (C154Y and R312H) of the human Kir2.1 channel involved in the Andersen-Tawil syndrome.

Dania Zuniga[1#*], Andreas Zoumpoulakis[1,2*], Rafael F. Veloso[1], Laurie Peverini[2], Sophie Shi[2], Alexandre Pozza[3], Valérie Kugler[4], Françoise Bonneté[3], Tahar Bouceba[5], Renaud Wagner[4], Pierre-Jean Corringer[2], Carlos A. H. Fernandes[1], Catherine Vénien-Bryan[1&]

[1] UMR 7590, CNRS, Muséum National d'Histoire Naturelle, IRD, Institut de Minéralogie, Physique des Matériaux et de Cosmochimie, IMPMC, Sorbonne Université, 75005 Paris, France

[2] Institut Pasteur, Université Paris Cité, CNRS UMR 3571, Channel-Receptors Unit, Paris, France

[3] Université Paris Cité, CNRS, UMR 7099, Laboratoire de Biochimie des Protéines Membranaires, Institut de Biologie Physico-Chimique, Paris 75005, France.

[4] IMPReSs Facility, Biotechnology and Cell Signaling UMR 7242, CNRS– University of Strasbourg, Illkirch, Cedex, France.

[5] Sorbonne University, CNRS, Institut de Biologie Paris-Seine (IBPS), Protein Engineering Platform, Molecular Interaction Service, F-75252 Paris, France

[#] present address: Cardiovascular Research Institute, University of California, San Francisco, California, USA.

* These authors contributed equally to this work.

[&]Correspondence: Catherine Vénien-Bryan (catherine.venien-bryan@sorbonne-universite.fr)

Abstract

Inwardly rectifying potassium (Kir) channels play a pivotal role in physiology by establishing, maintaining, and regulating the resting membrane potential of the cells, particularly contributing to the cellular repolarization of many excitable cells. Dysfunction in Kir2.1 channels is implicated in several chronic and debilitating human diseases for which there are currently no effective treatments. Specifically, Kir2.1-R312H and Kir2.1-C154Y mutations are associated with Andersen-Tawil syndrome (ATS) in humans. We have performed structural studies and have investigated the impact of these two mutants in the trafficking of the channel to the cell membrane and function in *Xenopus laevis* oocytes. Despite both mutations being successfully trafficked to the cell membrane and capable of binding PIP_2 (phosphatidylinositol-4,5- bisphosphate), the main modulator for channel activity, they resulted in defective channels that do not display K^+ current, albeit through different molecular mechanisms. Co-expression studies showed that R312H and C154Y are expressed and associated with the WT subunits. While WT subunits could rescue R312H dysfunction, the presence of a unique C154Y subunit disrupts the function of the entire complex, which is a typical feature of mutations with a dominant-negative effect. Molecular dynamics simulations showed that Kir2.1-C154Y mutation induces a loss in the structural plasticity of the selectivity filter, impairing the K^+ flow. Furthermore, the cryo-EM structure of the Kir2.1-R312H mutant cytoplasmic region confirmed previous findings that this mutation leads to a loss of the inter-subunit interaction network between residues R312, H221, and E303, thereby impairing channel gating at the G-loop level. Therefore, this study identified the molecular mechanisms by which two ATS-causing

mutations impact Kir2.1 channel function and provide valuable insights that can guide potential strategies for the development of future therapeutic interventions for ATS.

Introduction

Potassium channels are a very large family of integral membrane proteins that are ubiquitous with incredibly diverse physiological functions. There are more than 80 genes that code for K^+ channels in the human genome alone (Doupnik et al., 1995). The differences in their structures allow them to be regulated by various auxiliary subunits, to interact with different agonists, and to intervene at different stages of the action potential with diverse effects. Kir channels were first described in frog skeletal muscle as having an anomalous rectification (Katz, 1949) because their conductance decreased instead of increasing upon cell depolarization. Although outward Kir currents are much smaller than inward ones, under physiological conditions, the outward currents regulate the excitability and duration of repolarization in excitable cells like neurons and cardiac myocytes (Hibino et al., 2010). Kir channels are responsible for generating and propagating the action potential in excitable cells, regulating the heartbeat, maintaining salts and water balance, and regulating cell volume and muscle contraction. To fulfill these crucial biological roles, the gating of all eukaryotic Kir channels is directly controlled by a variety of intracellular messengers or regulatory lipids (Hibino et al., 2010)

The Kir channels family is classified into seven subfamilies (Kir1 to Kir7) with Kir2.1 being the protein product of the KCNJ2 gene (Hibino et al., 2010). Kir2.1 is expressed at high levels in the heart, skeletal muscle, and neural tissue, and Kir2.1 mutations are associated with various diseases (Reilly and Eckhardt, 2021). Kir2.1 channels are selectively modulated by the signaling lipid phosphatidylinositol 4,5-bisphosphate (PIP_2) (D'Avanzo et al., 2010a). Loss-of-function mutations in Kir2.1 channel cause Andersen-Tawil syndrome (ATS), a rare autosomal disorder characterized by developmental skeletal abnormalities, periodic skeletal muscle paralysis, as well as biventricular tachycardia with or without the presence of long QT (Nguyen et al., 2013; Plaster et al., 2001). On the other hand, gain-of-function mutations in Kir2.1 result in cardiac phenotypes, including atrial fibrillation, and short QT syndrome (SQT3), attributed to increased repolarization capacity and thus shortened cardiac action potentials (Hattori et al., 2012; Xia et al., 2005).

All Kir channels are tetrameric structures and are thought to assemble onto tetramers of identical or related subunits in the endoplasmic reticulum (ER) of cells (Deutsch, 2002). Kir channels control the passage of K^+ ions through the selectivity filter containing the conserved amino acids ^{142}TIGYG^{146} (Kir2.1 numbering) (Doyle et al., 1998). Kir channels share characteristic structural features: a large cytoplasmic domain (CTD) hosting the C- and N-termini and a transmembrane domain (TMD) containing a slide helix, a pore helix, a loop containing the K^+ ion selectivity filter and two transmembrane helices (M1 and M2) separated by an extracellular loop (Fernandes and Zuniga et al., 2022; Hager et al., 2021). In the Kir2.1 structure, the tetrameric assembly is mediated mainly through interactions involving the M2, selectivity filter, and pore helix at the TMD, as well as the G-loop, and regions 226-250, and

325-340 at the CTD. No inter-subunit disulfide bonds are involved in the tetrameric assembly (Fernandes and Zuniga et al., 2022).

The Kir2.1-R312H and Kir2.1-C154Y mutants were first identified in 2009 and have been reported as loss-of-function mutations responsible for ATS in humans (Sacconi et al., 2009). The residue R312 is located in the CTD (Figure 1A), near the G-loop and the PIP_2 putative binding site, but is not directly involved in the PIP_2 binding. Nevertheless, this mutant does not conduct K^+. In our previous study, this residue has been described as important for the signal transmission to the G-loop gating mechanism upon PIP_2 binding (Fernandes and Zuniga et al., 2022). In contrast, the residue C154 is located in the N-terminal of the M2 helix and forms the unique disulfide bond within the Kir2.1 structure with the C122 of the same chain (Figure 1A-B). The residues C122 and C154 are conserved in all eukaryotic Kir members (Figure 1C). The mechanism by which the C154Y mutation renders the channel deficient remains controversial. Previous studies have suggested that the C122/C154 disulfide bond in Kir2.1 appears to be necessary for the channel assembly, but less critical for function in an assembled channel (Cho et al., 2000; Leyland et al., 1999). Recently, deep mutational scanning (DMS) experiments on mouse Kir2.1 expressed in HEK293T cells have indicated that mutations in the C154 residue may disrupt cell surface expression to a certain extent but not function (Coyote-Maestas et al., 2022). On the other hand, the crystal structure of chicken Kir2.2 has suggested that this disulfide bond may indeed be significant for channel function (Tao et al., 2009). Moreover, studies on Kir3.2 channels have demonstrated that these cysteine residues are not essential for the correct processing and insertion of the channel into the membrane but are crucial for its function (Bannister et al., 1999). Intriguingly, all prior experiments performed in *Xenopus laevis* oocytes have shown that mutated C154Y channels are expressed at the membrane (Cho et al., 2000; Leyland et al., 1999).

Herein, we highlighted by different approaches that Kir2.1-C154Y and Kir2.1-R312H mutations do not impact channel trafficking to the membrane on *X. laevis* oocytes. Moreover, we have investigated the effects of these mutations on the structure and function of Kir2.1 channels by integrating results from electrophysiology experiments and structural data obtained through cryo-electron microscopy (cryo-EM) single-particle analysis and molecular dynamics (MD) simulations. In this paper, we propose two distinct molecular mechanisms associated with each studied mutation, both leading to the same pathology, ATS. The results presented here offer valuable insights into the intricate relationship between protein dysfunction and disease manifestation.

Results

Functional properties of Kir2.1-WT and mutants R312H and C154Y in *Xenopus* oocytes.

We studied the effects of replacing Arg312 with His (R312H) and Cys154 with Tyr (C154Y) on the K^+ current of Kir2.1 channels by recording two-electrode voltage clamp (TEVC) currents in *Xenopus laevis* oocytes (Figure 2). Upon injection of 50 ng of cDNA of the Kir2.1-WT, the oocytes showed classical currents with strong rectification properties (Figure 2, in dark blue). The oocytes injected with 50 ng of cDNA of the mutants R312H and C154Y

did not display observable currents and were indistinguishable from endogenous currents recorded from non-injected oocytes (Figure 2, in green and red on panels A and B, respectively).

To investigate whether the Kir2.1-R312H and Kir2.1-C154Y mutants were able to associate with WT subunits and form functional channels, we co-expressed Kir2.1-WT cDNA together with either mutant R312H or C154Y cDNAs (Figure 2). The current registered for oocytes injected with 50 ng of Kir2.1-WT cDNA was normalized to 100% activity in this study and used as a reference for all subsequent injections. The oocytes injected with 25 ng of Kir2.1-WT cDNA exhibit 40% current compared to the reference (Figure 2, in light blue). The coexpression of 25 ng of Kir2.1-WT cDNA with 25 ng of the Kir2.1-R312H cDNA exhibited 60% current compared to the reference, resulting in a 20% increase in activity compared to 25 ng of Kir2.1-WT cDNA alone (Figure 2A, in cyan). This indicates an increase of functional channels when the mutated Kir2.1-R312H is co-expressed with Kir2.1-WT, suggesting that WT subunits can rescue defective R312H channel subunits at certain ratios. Additionally, these data indicate that R312H does not affect the association of subunits to form tetrameric channels.

On the contrary, when 25 ng of Kir2.1-C154Y are co-expressed with the 25 ng of Kir2.1-WT, the current is decreased to 30% of the reference (70% decrease), which is 10% less than the 25 ng of Kir2.1-WT alone (Figure 2B, in magenta). This indicates a decrease in the number of functional channels when the mutated Kir2.1-C154Y is co-expressed with Kir2.1-WT. The consequence of the association of the WT with Kir2.1-C154Y mutant monomers is more dramatic than when Kir2.1-WT associates with the Kir2.1-R312H mutant monomers. The association between WT and C154Y mutant subunits is unable to restore the impaired function of the C154Y mutant; rather, the mutated C154Y subunits that associate with WT subunits disrupt the WT functionality.

Functional studies were also performed on the mutant H221R and the double mutant R312H/H221R (Figure S1A). Similarly to the results obtained with R312H and C154Y, the oocytes injected with 50 ng of cDNA of the mutants H221R and R312H/H221R did not display observable currents. However, the coexpression of 25 ng of Kir2.1-WT cDNA with 25 ng of the cDNA of the Kir2.1-H221R or Kir2.1-R312H/H221R mutants resulted in a 10% increase in activity compared to 25 ng of Kir2.1-WT cDNA alone (Figure S1A). The data show that these mutations allow the association of subunits to form tetrameric channels and the association with WT can rescue the dysfunctions caused by these mutations and their effects are similar to the single mutant R312H. Unpaired two-sided student t-test indicating the significance of the functional effect of the mutations on Kir2.1 channel current recorded by TEVC in *Xenopus laevis* oocytes are shown in Figure S1B-C.

Immunofluorescence experiments in *Xenopus* oocytes

To determine if the WT, R312H, and C154Y subunits of the Kir2.1 channel are transported to the cell membrane, or if they are retained within the cell, we performed immunofluorescence experiments in *Xenopus laevis* oocytes. Images were obtained with an epifluorescence microscope using an anti-Kir antibody (Figure 3A). The top four horizontal panels highlight the visualization of the orange-fluorescent Cyanine3 (Cy3) dye conjugated to the anti-Kir antibody which shows the location of Kir2.1. Compared to the negative control of GFP-only injected oocytes (top left image of the panel), expression of Kir2.1-WT and R312H and C154Y

mutants can be visualized in the membrane surface of the oocytes. The lower four panels show the superimposition of two colors: one emitted from the Cy3 conjugate, and the other emitted from the co-injected green fluorescent protein (GFP), which is used to confirm the successful injection of cDNA into the oocytes. The results show that the WT and mutant forms of the channel are expressed in the cell membrane of Xenopus oocytes, indicating that the mutations R312H and C154Y do not significantly impact the trafficking of the protein to the membrane in oocytes.

.

Expression and purification of the Kir2.1-WT and R312H and C154Y mutant forms

To obtain functional and structural information and perform biochemical and biophysical studies *in vitro*, Kir2.1-WT and both mutant forms were expressed in *Pichia pastori*s cells and purified following the protocol previously described (Fernandes and Zuniga et al., 2022). The Kir2.1-R312H mutant exhibited the same level of expression compared with Kir2.1-WT (data not shown) and showed the same size-exclusion chromatography (SEC) profile (Figure S2A). Although the Kir2.1-C154Y mutant did not affect the growth of *P. pastoris* cells, the protein yield was lower than the Kir2.1-R312H and Kir2.1-WT (less than 50%, data not shown). The SEC profile of the Kir2.1-C154Y mutant revealed a peak at the elution volume corresponding to aggregates and a small peak eluting at the same elution volume as the Kir2.1-WT tetramer (Figure S2A, in cyan). This small peak was used to conduct a native PAGE gel, which revealed that this fraction was polydisperse and consisted of aggregates and a faint quantity of tetramers (Figure S2B) in the absence of reducing agents. Kir2.1-C154Y mutant was not purified in sufficient quantity to perform SEC-MALLS-RI and cryo-EM analysis but enough for the SPR experiments.

Biotinylation assays: expression of the Kir2.1-WT and mutants on the cell surface

To verify that the Kir2.1-R312H and Kir2.1-C154Y mutants are trafficked to the plasma membrane in our expression system for purified hKir2.1, we evaluated the cell surface protein expression by biotinylation assays on whole *Pichia pastoris* cells (Figure 3B). After using a non-permeant reactant biotinylating primary amines at the cell surface, whole membrane proteins were further solubilized, purified, and analyzed using a horseradish peroxidase (HRP) -coupled extravidin probe. While the three Kir2.1-WT, Kir2.1-R312H, and Kir2.1-C154Y constructs were effectively produced and purified from the corresponding expressing clones (Coomassie blue stained SDS-PAGE, Figure 3B, left panel), all the samples submitted to the biotinylation assay were positively detected with extravidin-HRP reactant (Figure 3B, center panel), thus attesting on their presence at the surface of the treated cells These data support our previously obtained immunofluorescence results in *Xenopus* oocytes.

Evaluating the hydrodynamic radius of Kir2.1-WT in DDM detergent

The hydrodynamic radius (R_H) of the Kir2.1-DDM complex was evaluated to be 64.7 ± 1.3 Å (n=9) according to SEC measurements. This value agrees with the previously described Kir2.1 radius of 62.3 Å (D'Avanzo et al., 2010b). This slight discrepancy (within 1–3 Å) can be explained by any of the following differences in the two Kir2.1 protein samples used here

and in the previous study: protein expression in different heterologous systems (*P. pastoris* versus S. cerevisiae, respectively), employment of different constructs (His-tag, and FLAG-tag respectively), and purification using different detergents (DDM versus FC14 respectively), which may leave or remove different amounts of lipids surrounding Kir2.1.

Subsequently, dynamic light scattering (DLS) measurements were used for comparison. The auto-correlation curves of Kir2.1-WT followed the expected exponential decay with increasing delay time (data not shown), and the curves could be fitted using Dynamics V7 to determine the R_H and estimate the polydispersity level (%Pd) of the sample. DLS measurements provided an R_H of 60.8 ± 8.5 Å (n=6) for Kir2.1 with a weighted average polydispersity (%Pd) of 27.5% ± 9.8%. The %Pd gives an indication of the heterogeneity in the sample; the relative polydispersity of the sample is most likely due to the dynamic nature of the detergent.

In solution biophysical characterization of the Kir2.1-WT and R312H mutant by SEC-MALLS-RI

Kir2.1-WT solubilized in DDM

Size-exclusion chromatography coupled with multiple angle laser light scattering and differential refractive index (SEC-MALLS-RI) is a suitable technique to determine the absolute mass of the membrane protein-detergent complex, the respective mass fraction of protein, and detergent without the need for column calibration. Additionally, this technique allows the determination of the oligomeric state of the protein (Strop and Brunger, 2005). The SEC-MALLS-RI profile of the Kir2.1-WT shows a peak compatible with a tetramer at an elution volume of approximately 9.7 mL (Figure 4A). A closer examination of this peak showed that all signals (UV, LS, and ΔRI) aligned perfectly at its center (Figure 4B), allowing determination of the molar mass of the complex (for theoretical details, see supplementary data). In addition, protein conjugate analysis showed that Kir2.1 is extremely homogeneous throughout the peak in the buffer condition used, which includes 0.03% DDM (Figure 4B). The Kir2.1-DDM complex was determined to have a molar mass of 304.9 ± 0.9 kDa, with Kir2.1 contributing 203.9 ± 0.6 kDa and being surrounded by 100.1 ± 0.9 kDa of DDM. This corresponds to a tetrameric protein (theoretical Mw of monomer = 51.6 kDa) with approximately 194 ± 2 bound DDM molecules. The protein-free micelles that eluted at 14.1 mL had a mass of 76.4 ± 1.7 kDa, consistent with the published DDM micelle mass of 72 kDa and corresponding to an aggregation number (Nag) of 140 (Strop and Brunger, 2005).

Kir2.1-R312H mutant solubilized in DDM

The SEC-MALLS-RI analysis shows that the Kir2.1-R312H-DDM complex was also very homogeneous throughout the peak (Figure 4C-D). This enabled precise calculations of the molar mass of the complex, resulting in a value of 307 ± 4.4 kDa for the complex consisting of tetrameric Kir2.1-R312H with 206.8 ± 3.2 kDa molar mass and 100.3 ± 4.9 kDa DDM. The number of DDM molecules bound to the Kir2.1-R312H-DDM complex was 194 ± 9, similar to that of the Kir2.1-WT-DDM complex (194 ± 2). In conclusion, Kir2.1-R312H formed a homogeneous tetramer, like the Kir2.1-WT counterpart, and therefore, the R312 mutation did not affect the ability of Kir2.1 to form a tetramer.

Kir2.1-WT solubilized in FC14 followed by an exchange in DDM or PCC-Malt detergents

Previous work demonstrated that functional FLAG-tagged Kir2.1 could be successfully isolated from *S. cerevisiae* cells using 1% FC14 (tetradecyl-phosphocholine) (D'Avanzo et al., 2010b). For our construct, 0.5% FC14 provided excellent solubilization yields (Figure S3A). Purifying Kir2.1 exclusively in FC14 (0.03%) resulted in 55% of Kir2.1 being purified as tetramers (R_H = 60 Å) and 43% eluting as monomers (R_H = 31.3 Å) (Figure S3B, in yellow). Due to this high proportion of monomers, we attempted detergent exchanges with either 0.03% DDM (Kir2.1-FC14-DDM) or 0.03% PCC-Malt (4-trans-(4-trans-Propylcyclohexyl)-cyclohexyl α-maltoside) (Kir2.1-FC14-PCC-Malt). PCC-Malt is a detergent with a maltoside head like DDM, but the hydrophobic tail bears two cyclohexyls instead of a linear alkyl chain. It has been increasingly used recently and has been shown to increase membrane protein stability (Missel et al., 2021). After the detergent exchange, we recovered the SEC peak corresponding to the Kir2.1 tetramer (R_H = 62.8 Å) (Figure S3B, in purple). However, this sample formed aggregates when concentrated by a factor of ~ 25 (Figure S3B, in red). We analyzed further the properties of Kir2.1-FC14-DDM samples using SEC-MALLS-RI. The profile is shown in Figure S4A and is similar to Kir2.1 WT in DDM (Figure 4A), with the tetrameric peak eluting at the expected volume (~9.7 mL). However, we observed two noticeable differences: i) although all three signals (LS, ΔRI, and UV) were visible, they did not align (Figure S4B) indicating that the sample does not appear homogeneous along the peak. Consequently, we could not determine the absolute protein molar mass with accuracy; and ii) a depletion in the detergent LS and ΔRI signals was observed at 15 mL suggesting that the DDM is pumped from the mobile phase to the protein complex and the extra micelles (Figure S4A, red and blue curves). Protein-free FC14 micelles eluted at ~14 mL with an equal peak contribution from LS and ΔRI and minimal UV (Figure S4C). The depletion in the LS and ΔRI signals was also observed in the two controls, 5% FC14 and 5% FC14-DDM (Figure S4C). The detergent peak obtained in the sample (Figure S4A) eluted similarly to that of the FC14-DDM mixture, indicating an incomplete exchange of FC14 during the elution on the affinity column. Nonetheless, the depletion of DDM from the baselines implies that FC14 and DDM are miscible; therefore, a complete exchange could be possible under different exchange conditions, for instance, DDM concentrations should be significantly increased to displace FC14, which has a CMC slightly lower than DDM (0.12 mM and 0.17 mM respectively). Kir2.1-FC14-PCC-Malt samples were also investigated by SEC-MALLS-RI, and their profile was similar to that obtained with Kir2.1 FC14-DDM samples (Figure S5). The peak corresponding to Kir2.1 tetramers was obtained at the same elution volume (~9.7 mL) (Figure S5A). As for the Kir2.1-FC14-DDM samples, detergent signal depletion at 15 mL was also present (Figure S5A), although less pronounced than Kir2.1 FC14DDM. The three signals (LS, ΔRI and UV) did not align (Figure S5B) suggesting a detergent mixture around Kir2.1. The depletion in the LS and ΔRI signals was also observed in the two controls (5% FC14 and 5% FC14-PCC-Malt) (Figure S5C). These SEC-MALLS-RI experiments indicated an incomplete exchange of FC14 either with DDM or with PCC-Malt in Kir2.1 samples obtained from *Pichia pastoris* cells.

PIP_2 binding interaction with Kir2.1-C154Y mutant

The association and dissociation rate constants, k_{on} and k_{off}, respectively, and the dissociation constant (K_D) of the Kir2.1-C154Y mutant were determined directly from surface plasmon resonance. Kir2.1-C154Y was immobilized at 3900 to 6500 RU (response units) levels on CM5 sensor chips. Sequential injections of PIP_2 ranging from 1.25 μM to 20 μM were performed. The fitted curves of the interaction between Kir2.1-C154Y tetramer fraction with PIP_2 revealed that PIP_2 was able to bind to the mutant Kir2.1-C154Y (Figure 5) with no significant differences in kinetic parameters between C154Y (K_D = 6.98 ± 2.25 μM) and the WT (K_D = 3.2 ± 0.8 μM (Fernandes and Zuniga et al., 2022) suggesting that the C122/C154Y intra-subunit disulfide bond does not impact the PIP_2 binding. Likewise, previously obtained SPR results with the Kir2.1-R312H mutant also showed that the R312H mutation did not significantly affect the PIP_2 binding (Fernandes and Zuniga et al., 2022).

Cryo-EM structure of the CTD domain of the Kir2.1-R312H mutant

Our previous structural studies showed that the inter-subunit interaction network formed by salt bridges and like-charged contact pairs between the residues R312, H221, and E303 may play a pivotal role in allowing the conformational changes induced by PIP_2 for G-loop gating (Fernandes and Zuniga et al., 2022). Moreover, our molecular modeling of the R312H mutation suggested that this mutation would cause a complete loss of this interaction network (Fernandes and Zuniga et al., 2022). This finding is supported by an independent DMS analysis (Coyote-Maestas et al., 2022) that demonstrated a functional sensitivity in residues on the βCD loop (H221) and βEG loop (F262) and proposed a potential coupling with βH (I207) and βI (R312), and the G-loop. Furthermore, mutations in these regions were found to be detrimental to the proper function of Kir2.1 channels (Coyote-Maestas et al., 2022).

To confirm these results, we obtained here the cryo-EM structure of the CTD domain of the Kir2.1-R312H mutant at 5.3 Å resolution (Figures 6A and S6). Despite the modest global resolution, the resolution in the region of H312 is 4.1 Å (Figure S6), which allows proper identification of the sidechains. We made a comparative analysis between the CTD domain of the Kir2.1-R312H mutant (Figure 6A) and the Kir2.1-WT (Figure 6B) at the H312 vicinity. There is a significant decrease in the number of inter-subunit like-charged contact pairs between the residues at positions 221 and 312, and all E303-mediated salt bridges are lost. In the Kir2.1-WT structure, the residue E303 establishes salt bridges with H221 and R312 residues within the 3.4-3.7 Å distance range (Figure 6B, dashed red line). In the Kir2.1-R312H structure, the distances between the oxygen and nitrogen atoms capable of establishing salt bridges from E303 to H221 and H312 are in the distance range of 13-16 Å (Figure 6B, dashed black line). Similarly, there is a decrease in inter-subunit like-charged contact pairs between the residues at positions 221 and 312. In the Kir2.1-WT structure, 1 to 3 of such interactions are observed in each chain, the Kir2.1-R312H structure exhibits only one in three of the four chains (Figure 6A-B). In conclusion, the R312H mutation significantly impairs the inter-subunit interaction network formed by R312, H221, and E303 residues, this finding confirms our previous *in silico* results.

To assess the potential for recovering the intersubunit network between R312, H221, and E303 residues, we modeled the double mutant H221R/R312H using Chimera software, followed by local energy minimization (Figure 6C). The H221R/R312H double mutation did

not recover this interaction network. Similarly to the R312H mutant, the salt bridges remain disrupted, and only a few like-charged pair contacts between R and H residues were regained. The distances between the oxygen and nitrogen atoms able to establish salt bridges from E303 to R221 and H312 are in the distance range of 6.1-8.2 Å. Additionally, the inter-subunit like-charged contact pairs between the residues at positions R221 and H312 were not recovered; like the R312H counterpart, only one interaction of this type was observed in the four chains (Figure 6C).

MD simulations on Kir2.1-WT and Kir2.1-C154Y mutants

Structural analysis of the C122/C154 disulfide bond reveals its role in establishing a structural connection from the selectivity filter and the 147-153 loop to the extracellular loops (Figure 7A), which may be disrupted when the disulfide bond is broken (Figure 7B**)**. To evaluate the impact of the C154Y mutation on the structure of the Kir2.1 channel, we performed molecular dynamics (MD) simulations on the cryo-EM structure of Kir2.1 (PDB ID 7ZDZ (Fernandes and Zuniga et al., 2022) incorporating the C154Y mutation in all four subunits of the Kir2.1 tetramer (Chains $ABCD_{C154Y}$). Moreover, we also explored hybrid tetrameric WT-C154Y structures by placing the C154Y mutation in i) three subunits (Chains ABC_{C154Y}, Chain D_{WT}), ii) two adjacent subunits (Chains AB_{C154Y}, Chains CD_{WT}), iii) two diagonally opposite subunits (Chains AC_{C154Y}, Chains BD_{WT}), iv) one subunit (Chain A_{C154Y}, Chains BCD_{WT}). The protein structure was embedded in a 1-palmitoyl-2-oleoyl-sn-glycero-3-phosphocholine (POPC) lipid bilayer and the MD simulations were performed for 200 ns in triplicate.

Firstly, we assessed the impact of the C154Y mutation on the root mean square fluctuation (rmsf) of residue 154, the 147-153 loop, and the selectivity filter (residues 142-146) along the MD simulations (Figure 7C-E and Table 1). The all-WT tetramers showed rmsf values of 2.22 ± 0.14 at C154, 2.01 ± 0.12 at the 147-153 loop, and 2.02 ± 0.18 at the selectivity filter. The all-C154Y structures showed a decrease in rmsf for Y154 (1.74 ± 0.17), 147-153 loop (1.63 ± 0.13), and selectivity filter (1.23 ± 0.05), with a more pronounced effect on the latter one (Figure 7C-E and Table 1). The extracellular loops are the most flexible regions of the Kir2.1 structure, as demonstrated by our previous MD simulations results (Fernandes and Zuniga et al., 2022). The decrease in rmsf of the 147-163 loop and the selectivity filter in the C154Y structure suggests a decrease in the flexibility of the selectivity filter when the C122/C154 bond is disrupted, suggesting that the break of the C122/C154 disulfide bond interrupts the structural connection between the extracellular loop and the selectivity filter. Interestingly, in the MD simulations performed with the hybrid WT-C154Y structures, the WT subunits also exhibit a decrease of the rmsf of the 147-153 region (~1.7-1.9) and selectivity filter (1.6-1.8) (Figure 7C-E and Table 1). These data imply that the impact of mutation in one subunit can affect the others, highlighting the required cooperativity of the selectivity filter in the tetramer to allow the flow of K^+ ions.

Then, we investigated in detail the effect of breaking the disulfide bond on the selectivity filter structure. In a previous study on KcsA channels, it was demonstrated that the loss of flexibility of the selectivity filter leads to non-functional K^+ channels. This loss prevents the attainment of dihedral angle values of the amino acids from this region that would favor the K^+ ion flow (Valiyaveetil et al., 2004). We assessed the impact of the decreased rmsf values,

caused by the C154Y mutation, by evaluating the occurrence frequency of dihedral angles of the selectivity filter residues: T142, I143, and Y145 along the MD simulations (Figure 8, Table 2, and Figures S7, S8 and S9). The MD simulations performed with Kir2.1-WT and Kir2.1-C154Y mutant revealed three main populations of dihedral angle frequencies for residues T142 and Y145. For residue T142, the most frequent dihedral angles range from −40° to −30° (brown), −20° to −10° (cyan), and 30° to 40° (green) (Figure 8A); whereas for Y145, dihedral angles range from −30° to −20° (brown), −10° to 0° (cyan), and 30° to 40° (green) (Figure 8B). In the MD simulations performed with the Kir2.1-C154Y mutant, a significant decrease in the frequency of the dihedral angles in the 30° to 40° range is observed in both residues (Figure 8A-B, Table 2, and Figures S7 and S8).

The WT subunits from the all-WT structure exhibit 16% and 18% frequency of a dihedral angle within the 30° to 40° range for the T142 and Y145 residues, respectively. In contrast, the C154Y-containing subunits show a decreased frequency, ranging from 0.1 to 3.4% (Table 2). This reduction in the frequency of dihedral angles within the 30° to 40° range for these residues in the chains containing the C154Y mutation is counterbalanced by an increase in the frequency of dihedral angles within the −20° to −10° range. Interestingly, this decrease in dihedral angle frequency in the 30° to 40° range is also observed for the T142 and Y145 residues of the WT subunits in the hybrid WT-C154Y structures. However, this effect is less pronounced in the hybrid structures where the C154Y mutation was placed in two diagonally opposite subunits (Chains AC_{C154Y}, Chains BD_{WT}), and in one subunit (Chain A_{C154Y}, Chains BCD_{WT}) (Table 2 and Figures S7 and S8). The orientation of the side chains of the T142 and Y145 residues in the three main popuations of dihedral angle frequencies observed along MD simulations is illustrated in Figure 8C-D.

Concerning I143, in the Kir2.1-WT structure, and the Kir2.1-C154Y mutant, the most frequent dihedral angles range from −45° to −30° and 30° to 40° (Figure 8E). However, the mutant structure (all four C154Y subunits) shows a decrease in the frequency of dihedral angles within the 30° to 40° range compared to the WT subunits. Note that the impact in the dihedral angle frequencies is less pronounced than in the T142 and Y145 residues (Table 2 and Figure 8E). However, this phenomenon is not evident when analyzing the hybrid WT-C154Y structures (Table 2 and Figure S9). Therefore, the impact of the C154Y mutation on the dihedral angles of the I143 residue remains inconclusive.

Additionally, given the potential steric hindrance caused by the C154Y mutation, we explored the effect of the C154S mutation placed on four chains of the Kir2.1 structure on the plasticity of the selectivity filter and frequency of dihedral angles. The results for C154S were similar to those obtained for C154Y (Figure S10A and Table S1). Previous attempts to restore interactions between C122 and C154 by replacing these residues with aspartate and lysine, respectively, did not rescue the channel function (Cho et al., 2000). Here, we attempted to restore these interactions by replacing C122 and C154 with tyrosines (C122Y/C154Y) or tryptophans (C122W/C154W), by exploring the potential of the side chains in establishing aromatic-aromatic interactions. We did not observe any rescue of the rmsf or the dihedral angle frequency in the 30° to 40° range for the T142 and Y145 residues (Figure S10B-C and Table S1). These data indicate that only strong interactions between C122 and C154 residues, such as

a covalent bond established in a disulfide bridge, would be able to maintain the structural connection between the extracellular loops and the selectivity filter.

Discussion

The Kir2.1 channel undergoes many steps before it can conduct K^+ ions. It must be properly recognized and targeted to the endoplasmic reticulum, folded, tetramerized, and trafficked to the plasma membrane. The mature channel must be able to interact with its modulators and effectively gate: open and close. The open state is triggered by the binding of PIP_2 that induces several conformational changes in the channel (Hansen et al., 2011; Hibino et al., 2010; Tao et al., 2009). Any genetic alteration in the DNA coding region can hamper any of these stages, affect the function and dynamics of the protein, and lead to pathology. Even when the genetic basis of a disease may be known, the molecular mechanisms driving the dysfunction remain elusive (Bergendahl et al., 2019). A more comprehensive understanding of these molecular mechanisms has the potential to improve the diagnosis and treatment of human genetic disorders.

The dominant negative effect of the C154Y mutation arising from loss in the structural plasticity of the selectivity buffer

C154, a residue conserved in all eukaryotic Kir members, is located in the N-terminal of the M2 helix at the membrane interface. This residue establishes a disulfide bond with C122, which connects the extracellular loops to the selectivity filter towards the 147-153 loop (Figure 1B-C). Three mutations at the C154 residue are responsible for ATS in patients: C154F (Bendahhou et al., 2005) C154Y (Sacconi et al., 2009), and C154G (ClinVar RCV001901246.2). Moreover, other studies evaluating the C154A and C154S mutations also showed that these mutations abolished the current in *Xenopus laevis* oocytes (Cho et al., 2000; Leyland et al., 1999). Attempts to disrupt this disulfide bond by applying reducing agents (10-20 mM DTT or 10 mM reduced glutathione) extracellularly to cells expressing wild-type Kir2.1 showed minimal impact on channel currents (Cho et al., 2000; Leyland et al., 1999). However, the crystal structure of the Kir2.2 channel was obtained in the presence of 20 mM DTT and 3 mM TCEP reducing agents, and this disulfide bond remained unaffected (Tao et al., 2009). This suggested that the C122/C154 disulfide bond can withstand moderate concentrations of reducing agents and that this disulfide bond should be significant for the channel function (Tao et al., 2009).

Our immuno-fluorescence experiments in *X. laevis* oocytes and analysis of surface biotinylation of membrane proteins on *P. pastoris* cells show that the Kir2.1-C154Y mutant is expressed and trafficked toward the cell membrane (Figure 3A-B) However, expression of this mutant in *X. laevis* oocytes resulted in no detectable currents (Figure 2), although this mutation did not impact the PIP_2 binding (Figure 5). Moreover, our data show that the mutant Kir2.1-C154 subunits can assemble into a complex when expressed with Kir2.1-WT subunits (Figure 2B). Therefore, the C154Y mutation in Kir2.1 channels does not affect the association of subunits into multimeric complexes but leads to an impairment of the channel function. The association with WT subunits does not rescue C154Y dysfunction; instead, the mutant C154Y subunits that associate with WT subunits disrupt the function of the channel. This a

characteristic feature of mutations with dominant-negative effect, where the mutant subunit 'poisons' the activity of the hybrid WT-mutant complex, resulting in a disproportionate loss of function, as most of the complexed assemblies would contain at least one mutant subunit (Bergendahl et al., 2019; Gerasimavicius et al., 2022). Based on a probability model previously proposed for mutations with dominant-negative effect in homomeric complexes (Bergendahl et al., 2019), we proposed a model of the association between C154Y and WT subunits in hybrids WT-C154Y Kir2.1 complexes (Figure 9A). According to this model, a unique mutated subunit disrupts the function of the entire complex and can lead to a loss of function of 93.75%. Note that this value is correct if the WT and mutated subunits are expressed in the same amount. In our case, when Kir2.1-C154Y is co-expressed with Kir2.1-WT we observed a loss of function of 70% (Figure 2B), a value that is higher than any other expected loss-of-function model but is less than the theoretical 93.75%. This can be explained by the fact that, although the same amount of Kir2.1-WT and Kir2.1-C154Y cDNA were injected, Kir2.1-WT is more readily expressed than Kir2.1-C154Y. Therefore, more WT subunits would be available for association, leading to a higher current than expected.

Mutations in residues C122 and C154 to serine in Kir2.3 channels (C113 and C145 according to Kir2.3 numbering) provided the same results in *X. laevis* oocytes: the mutant channels were expressed, assumed to be processed into tetramers, and trafficked to the membrane, but in a non-functional form (Bannister et al., 1999). Whole-cell and single-channel currents in *X. laevis* oocytes of C122S and C154S mutants in Kir2.1 channels revealed that the presence of a single mutant subunit was enough to abolish the function of the tetrameric channel (Cho et al., 2000). Similarly, studies of the Kir2.1-C154F mutant in HEK293 cells demonstrated that this mutant traffics to the membrane and also exerts a dominant negative effect (Bendahhou et al., 2005). Our results also indicate that mutations leading to the disruption of the C122/C154 disulfide bond exert a dominant negative effect to abolish the Kir2.1 channel current.

To understand the molecular basis for this dominant negative effect, we explored the structural properties of the region around the C154 in the Kir2.1 structure. Our MD simulations showed that the C154Y mutation resulted in a decrease in the rmsf of the selectivity filter and a reduction in the frequency of dihedral angles in the 30° to 40° range for the T142 and Y145 residues located in this region (Tables 1 and 2; Figures 8, 9, S7 and S8). These data indicate that the disruption of the C122/C154 disulfide bond interrupts the structural connection between the flexible extracellular loops and the selectivity filter, resulting in a loss of structural plasticity of the selectivity filter and impairing the K^+ flow. Interestingly, even the mutation of C154 to the flexible residues alanine and serine did not recover the current in Kir channels (Cho et al., 2000; Leyland et al., 1999). Our MD simulations of the C154S mutation placed in four chains of the Kir2.1 structure provided similar results in terms of the structural plasticity of the selectivity filter (Figure S10A and Table S1). This indicates that only the flexibility level provided by the extracellular loops can provide the proper structural plasticity of the selectivity filter to allow the K^+ flow.

Notably, the decrease of rmsf of the selectivity filter and in dihedral angles in the 30° to 40° range for the T142 and Y145 residues was observed even in the WT subunits of the hybrid WT-C154Y structures (Tables 1 and 2; Figures 8, S7 and S8). These data highlight the cooperative role of the four subunits in coordinating the K^+ flow at the selectivity filter. Thus,

even only one mutated subunit can affect the tetrameric complex. In other words, for the C154Y mutation, all the subunits forming the channel must be functional to form an ion-conducting pore. Similar behavior was observed in HCN1 protein with a mutation at the pore (Xue et al., 2002). The presence of one such dominant-negative monomeric subunit suffices to render the entire channel complex nonfunctional.

Effect of the mutation R312H on the gating mechanism at the G-loop level

Our previous structural studies on Kir2.1 (Fernandes and Zuniga et al., 2022) describe a well-connected interaction network between the PIP_2-binding site residues, R218 and K219, and the G-loop region (E303) via residues R312 and H221. Our data suggest that the conformational changes required for the G-loop opening are most likely controlled by PIP_2 binding. Our previous *in silico* data shows that the replacement of R312 with histidine leads to a complete loss of the interaction network described above, this hypothesis is now supported by the cryo-EM structure of the CTD domain of the Kir2.1-R312H mutant (Figure 6). The interaction network integrity between subunits seems necessary for the proper allosteric transmission of the signal between R312 and the G-loop of the adjacent subunit upon PIP_2 binding, which possibly could allow the release of the constriction point on the G-loop and the flow of K^+. We attempted to restore the interaction network between the residues 221, 303, and 312 by performing electrophysiological and molecular modeling analysis of the double mutant H221R/R312H. This double mutation did not recover this interaction network (Figure 6) and was not able to rescue the normal Kir2.1 current (Figure S1A). These results confirm that the structural integrity of this inter-subunit network of interactions, especially the E303-mediated salt bridges with R312 and H221 residues, is essential for proper G-loop gating.

Our immuno-fluorescence experiments in *X. laevis* oocytes and analysis of surface biotinylation of membrane proteins on *P. pastoris* cells show that R312H mutants are expressed and trafficked toward the cell membrane (Figure 3A-B). Expression of this mutant in *X. laevis* oocytes resulted in no detectable currents (Figure 2), although this mutation did not significantly impact the PIP_2 binding as previously shown (Fernandes and Zuniga et al., 2022). The coexpression of Kir2.1-WT and R312H mutant in *X. laevis* oocytes resulted in a partial recovery of channel current, indicating that the dysfunction caused by R312H mutation can be partially rescued by association with the WT counterpart (Figure 2A). Moreover, these data suggest that a partially open state of the channel at the G-loop level resulting from the association between WT and R312H mutated subunits can provide K^+ current.

Based on a probability model previously proposed (Bergendahl et al., 2019), we modeled the effect of all combinations on the association of R312 and WT subunits along with their respective loss-of-function probabilities (Figure 9B). The difference in the loss-of-function probability arises from the position of the two mutated subunits within the tetramer complex. If side-by-side mutant subunits are non-functional, a theoretical loss of function of 56.25% is predicted (Figure 9B, upper panel). If diagonally opposed mutant subunits are dysfunctional, then the probability of loss of function is 43.75% (Figure 9B, lower panel). Alternatively, when any positioning of two mutant subunits results in non-functionality, the loss-of-function probability increases to 68.75%. Our electrophysiology results show a 40% loss of function when R312H and WT subunits are co-expressed compared to when only WT

subunits are expressed (Figure 2A). Therefore, based on the loss-of-function prediction probabilities (Figure 9B), these results suggest that diagonally opposed mutant subunits lead to a loss of function, while side-by-side mutant subunits remain functional. Based on this observation, we propose a structural hypothesis to understand this phenomenon (Figure S11). When the R312H mutation is placed in two diagonally opposite subunits, the G-loops of the R312H-containing subunits close the center of the channel pore, resulting in a nonfunctional channel. In contrast, when the R312H mutation is placed on side-by-side subunits, part of the channel pore remains unblocked, allowing the K^+ flow even in this partially open state of the G-loop (Figure S11).

Stability of WT and mutated complexes after extraction from the membrane

We obtained homogeneous tetramers of Kir2.1-WT when expressed in *Pichia pastoris* cells and solubilized in DDM detergent, as indicated by SEC and SEC-MALLS-RI data (Figures 4 and S2). Moreover, using SEC-MALLS-RI, we determined the number of DDM molecules bound to the TMD of Kir2.1 after membrane extraction. Good solubilization yields were also obtained using 0.5% FC14 detergent; although a significant dissociation of the Kir2.1 tetramers into monomers was observed (Figure S3). The exchange of FC14 for the detergents DDM and PCC-malt successfully recovered the tetramers. However, SEC-MALLS-RI data revealed an incomplete exchange, with a mixed belt of detergent (FC14-DDM or FC14-PCC-Malt) remaining around the protein. Indeed, the exchange between detergents poses challenges around sample preparation, as different methods have varying efficiencies, and detergents exhibit distinct CMC and TMD binding properties. Consequently, they do not have the same ability to be exchanged (Levesque et al., 2023). Therefore, quality control of the protein-detergent environment is required to ensure sample homogeneity and the correct oligomeric state of the protein. In this context, the biophysical data presented here demonstrate that SEC-MALLS-RI is a highly suitable technique for evaluating the molecular mass of the protein oligomers, the physicochemical heterogeneity of protein–detergent complexes, and determining the minimum amount of detergent required to maintain protein stability.

SEC and SEC-MALLS-RI data showed that the Kir2.1-R312H mutant formed a homogeneous tetramer, indicating that this mutation did not impair the correct oligomerization of the channel (Figures 4 and S2). Contrastingly, upon purification, the Kir2.1-C154Y mutant exhibited reduced structural stability and increased susceptibility for aggregation (Figure S2). On the other hand, TEVC data obtained from *Xenopus laevis* oocytes and by biotinylation of *Pichia pastoris* cell membranes (Figures 2 and 3) show that Kir2.1-C154Y mutant is normally trafficked to the cell surface. These data indicate that the aggregation phenomenon observed *in vitro* may not be present *in vivo*. Two factors could be related to this observation. Firstly, during expression and purification, the protein is diluted in an aqueous buffer lacking the crowed cell environment, which may provide different types of interactions (Despa et al., 2005) that can contribute to the stability of this mutant. Secondly, when Kir2.1 is embedded in a cell membrane, only C122, C149, and C154 residues, located in the extracellular region are capable of forming disulfide bonds. Upon solubilization in DDM, the previously inaccessible intracellular cysteines become theoretically accessible to form disulfide bonds with the free C122 in the vicinity, potentially leading to protein aggregation.

Conclusion remarks

ATS poses a significant challenge in terms of therapeutic intervention as, to date, there is no effective treatment for this disease. Understanding molecular mechanisms can provide a pathway toward treatment. Therefore, understanding how ATS-causing mutations affect the Kir2.1 channel function at the molecular level provides a crucial foundation for designing targeted drugs to rescue the impaired function of these channels. Here, we were able to identify the molecular mechanisms by which two ATS-causing mutations (C154Y and R312H) affect the function of these channels. Both mutations did not affect the channel trafficking to the cell membrane; however, they impair the channel function, even though they can bind to the lipid activator PIP_2. Notably, they hinder the channel function by different mechanisms. The R312H mutation impairs the gating mechanism at the G-loop level, while the C154Y mutation impacts the K^+ flow at the selectivity filter. We also observed that C154Y has a more drastic effect on the Kir2.1 channels than the R312H loss-of-function mutation. Our data support that C154Y exerts a negative dominant effect, as the presence of this mutation in a single subunit of the tetramer is sufficient to render the entire complex nonfunctional. On the other hand, Kir2.1 channels containing R312H mutation in one or two adjacent subunits can still maintain channel current.

Our data can offer valuable insights that can guide potential strategies to rescue the function of both mutations. For the R312H mutation, compounds targeting the enhancement of the stability in the intersubunit interaction network between E303, H221, and H312 could potentially correct the gating abnormalities and restore normal channel function. Alternatively, gene therapy to increase the available wild-type protein would also result in increased currents. In the case of the dominant negative C154Y mutation, drug design should focus on the extracellular regions of the protein or directly on its selectivity filter. Compounds capable of reestablishing the structural connection between the extracellular loops and the selectivity filter, or providing increased flexibility and structural plasticity to the selectivity filter could potentially alleviate the hindrance to K^+ flow caused by this mutation.

Materials and methods

hKir2.1 synthetic genes and expression in *Pichia pastoris* cells and *Xenopus laevis* oocytes

Protein expression in *Pichia pastoris.*

Protein expression was handled as previously described (Hartmann et al., 2016) (Fernandes and Zuniga et al., 2022). Briefly, synthetic KCNJ2 genes encoding residues 1 to 427 (the whole sequence Uniprot reference P63252) of human Kir2.1 WT, R312H, or C154Y mutants optimized for expression in yeast were cloned in a pPIC9K vector upstream of a sequence coding for a PreScission protease cleavage site (LEVLFQGP) followed by a linker of 11 amino acids and a 10His tag (GenScript). The plasmids were introduced in *Pichia pastoris* strain SMD1163 (*his4, pep4, prb1*), and the resulting colonies were further analyzed *via* an *in situ* Yeastern blot immunoassay in order to identify the best-expressing clones. Protein production was performed as previously described (Fernandes and Zuniga et al., 2022). Cells were harvested by centrifugation, washed in PBS buffer (pH 7.4), and stored at −80 °C until use.

Protein expression in *Xenopus laevis* oocytes

The hKir2.1 cDNA gene coding the sequence of human Kir2.1 was cloned into the mammalian expression vector pMT3 containing an Ampicillin resistance gene (GenScript). Kir2.1 pathological mutants (C154Y, R312H) were generated by polymerase chain reaction (PCR) with synthetic primers using the CloneAmp HiFi PCR Premix (Takara). Primer sets used for site-directed mutagenesis were the forward sequence '5-GTGACTGATGAGTACCCAATTGCAGTGTTTATGGTG -3', and the reverse sequence '5-CCACCATAAACACTGCAATTGGGTACTCATCAGTCAC -3' for C154Y, the forward sequence '5- CTCAGTGTCACTCTAGCTATCTGGC -3' and the reverse sequence '5-GCCAGATAGCTAGAGTGACACTGAG -3' for R312H, respectively (underlined nucleic acids indicate the mutated site). Mutations and DNA constructs were confirmed by sequencing (Eurofins, Cologne, Germany). *Xenopus laevis* oocytes at stage VI were provided by the University of Paris Saclay (TEFOR Paris-Saclay CNRS UAR2020/INRAE UMS 1451) and kept in Barth's solution (87.34 mM NaCl, 1 mM KCl, 0.66 mM $CaNO_3$, 0.75 mM $CaCl_2$, 0.82 mM $MgSO_4$, 2.4 mM $NaHCO_3$, 10 mM HEPES and pH adjusted at 7.6 with NaOH). Oocytes were dissociated from ovary segments by digestion in 1 mg·mL^{-1} collagenase type II (Gibco) dissolved in OR2 solution (85 mM NaCl, 1 mM $MgCl_2$, 5 mM HEPES, pH adjusted to 7.6 with KOH) for 1-2 h at room temperature under gentle agitation. Defolliculated oocytes were rinsed extensively with Barth's solution and thereafter stored at 4 °C in Barth's solution until required. Single oocytes were injected with 50 ng·µL^{-1} of cDNA coding for the monomeric sequence of hKir2.1, together with a cDNA encoding eGFP at 25 ng·µL^{-1}, into the oocyte nucleus by air injection. Injected oocytes were incubated at 18 °C in Barth's solution for 2-3 days for heterologous expression. In the case of co-expression of Kir2.1 wild-type and pathological mutants (C154Y, R312H), equal amounts (50 ng·µL^{-1}) of mutants and wild-type cDNA were injected.

Two-electrode voltage clamp (TEVC) recording in *Xenopus laevis* oocytes

Macroscopic potassium currents (whole-cell currents) were recorded 2-3 days after injection of hKir2.1 cDNA (Genscript) using a two-electrode voltage-clamp amplifier (OC-

725C, Warner Instruments) and Clampex 10.6 software (Molecular Devices) for data acquisition. Oocytes were perfused at room temperature with KD10 solution (10 mM KCl, 88 mM NaCl, 1.8 mM $CaCl_2$, 1 mM $MgCl_2$, and 5 mM HEPES, pH adjusted to 7.4 with NaOH. Voltage-sensing and current-recording glass microelectrodes were filled with 3 M KCl and pulled to be used at resistances between 0.2-2 MΩ. Currents were elicited by 500 ms pulses from −150 to +30 mV in 10 mV increments from a holding potential of −60 mV. Recorded currents were digitized at 500 Hz using a Digidata 1550A interface (Molecular Devices) and filtered at 100 Hz. No leak subtraction was performed during the experiments. Data analysis was performed with Clampfit 10.6 software (Molecular Devices). In all figures, statistical data are presented as mean ± S.E.M., where n represents the number of oocytes recorded. Co-injection of the pMT3 plasmid carrying the eGFP fluorescent protein was used to check that the injection of the cDNA was performed successfully. Fluorescent oocytes were the indication of a successful injection of the plasmid.

Immunofluorescence experiments in *Xenopus laevis* oocytes

For oocyte immunofluorescence experiments, GFP-positive oocytes were fixed in 4% paraformaldehyde (PFA) in phosphate-buffered saline (PBS) overnight at 4 °C. Fixed oocytes were washed two times with PBS for 5 min each and then treated with 0.1% Triton X-100 in PBS for 10 min for permeabilization. Non-specific staining was blocked using 10% horse serum in PBS for 30 min at room temperature, followed by two washes with 2% horse serum in PBS for 5 min each. For immunolabeling, oocytes were incubated with the Rabbit anti-Kir2.1 primary antibody (1:200, Alomone Labs) in 2% horse serum for 1 h 30 min at room temperature and washed two times with 2% horse serum for 5 min each. Oocytes were labeled with the Cy3-conjugated anti-Rabbit secondary antibody (1:300, Invitrogen) in 2% horse serum for 1 h at room temperature and washed with 2% horse serum for 5 min. After 2 h fixation in 4% PFA in PBS at 4 °C, oocytes were placed in 3% low-gelling temperature agarose overnight at 4 °C. 40 µm slices of each oocyte were made using a Leica VT1000 S vibratome (Leica BioSystems). Several slices per oocyte (7-9 slices per two oocytes, three separate experiments) were mounted on a microscope slide with the ProLong™ Diamond Antifade Mountant (Invitrogen) and analyzed using an epi-fluorescence microscope with constant exposure time for visualization of cell surface expression. GFP-injected oocytes were used as negative controls. Oocytes injected with the pMT3 plasmid coding for the human glycine receptor (GlyR) were used as positive controls, following the same protocol as for hKir2.1, but with a mouse anti-GlyR primary antibody (1:500, Synaptic Systems) and a Cy3-conjugated anti-mouse (1:300, Life Technologies) secondary antibody.

Cell surface protein biotinylation of *Pichia pastoris* cells

The biotinylation assays consisted in labeling cell surface proteins with a biotin reagent before lysing the cells and purifying the targeted proteins. Briefly, Kir 2.1-WT and mutants were expressed in yeast cells as previously described (Fernandes and Zuniga et al., 2022). Yeast pellet (4 g) was resuspended in 10 mL PBS buffer (137 mM NaCl, 2.7 mM KCl, pH 8, 8 mM Na_2HPO_4, and 2 mM KH_2PO_4) supplemented with 10 mM of Sulfo-NHS-LC-Biotin (Thermo Fisher) and incubated for 30 min with agitation at room temperature. The cells were then

washed three times with the PBS buffer and subjected to cell lysis, protein extraction, and purification as previously described (Fernandes and Zuniga et al., 2022). Proteins were analyzed on 10% gels SDS-PAGE either directly stained with Coomassie blue or electroblotted. Western blot membranes were incubated overnight at 4 °C, using either Extravidin-HRP (Sigma) at 1/1000 dilution in 10 ml of PBS-T buffer (PBS 1x, Tween20 0.02%, Milk 5%), targeting biotin, or an anti-Histidine conjugated with peroxidase at 1/1000 dilution in 10 mL of PBS-T buffer targeting His-tag Kir-2.1 (WT and mutants). The signal was revealed using the SuperSignal West PICO Plus kit (Thermo Fisher) and detected using Imager 680 (Amersham) with a 10-second exposition period.

Protein solubilization and purification in DDM or FC14 detergents

Purification of Kir2.1-WT and mutants (R312H and C154Y) was performed in DDM (n-Dodecyl-β-D-maltoside, Glycon), as previously described (Fernandes and Zuniga et al., 2022). Briefly, yeast cells were ruptured using either Constant System Cell Disrupter or FastPrep 24 (MP Biomedicals). The membrane proteins were solubilized by adding 29.3 mM DDM (1.5%). The purification process involved an affinity chromatography step using cobalt affinity resin (TALON, Clontech), followed by a size exclusion chromatography (SEC) on either a Superdex® 200 (10/300) GL column or Superdex® 200 Increase (10/300) column (Cytiva) pre-equilibrated with TKED buffer (20 mM Tris-HCl pH 7.4, 150 mM KCl, 1 mM EDTA, 0.03%/0.59 mM DDM) using the Äkta Purifier system (Cytiva). Fractions corresponding to the tetramer were pooled, 2 mM DTT, was added, and concentrated to 0.7–1 $mg \cdot mL^{-1}$. For extraction and purification using FC14 (tetradecylphosphocholine), the same protocol was used, but with a different buffer composition: 0.5% FC14 instead of 1.5% DDM for protein solubilization and 0.03% FC14 instead of 0.03% DDM for the purification steps. The exchange of Kir2.1 solubilized and purified in FC14 (Kir2.1-FC14) to DDM (Kir2.1-FC14-DDM) and PCC-Malt (4-trans-(4-trans-Propylcyclohexyl)-cyclohexyl maltoside from Glycon) (Kir2.1-FC14-PCCMalt) was performed as follow: after solubilization in 0.5% FC14, 20-30 CV of buffer containing DDM 0.05% or PCC-Malt 0.05% was added to the Kir2.1 immobilized in a cobalt affinity resin, followed by the usual elution and SEC steps in 0.03% DDM (Kir2.1 FC14-DDM) or 0.03% PCC-Malt(Kir2.1 FC14-PCC-Malt).

Determination of hydrodynamic radius by size exclusion chromatography

The hydrodynamic radius of the Kir2.1-DDM complex was determined using standard size exclusion chromatography using Superdex® 200 (10/300) GL and Superdex® 200 (10/300) Increase(Cytiva) columns equilibrated with TKED buffer (20 mM Tris-HCl pH 7.4, 150 mM KCl, 1 mM EDTA, 0.03%/0.59 mM DDM) at 0.3 $mL \cdot min^{-1}$ at room temperature. A high molecular weight gel filtration calibration kit (Gel filtration HMW Calibration kit, Cytiva) was used. The retention volumes for each standard and sample were measured and used to calculate the partition coefficients (K_{av}), defined as $K_{av}=(V_e-V_0)/V_t-V_0)$, where V_e is the elution volume, V_0 is the void column, and V_t is the total volume of the column. The hydrodynamic radius R_H of the human Kir2.1-DDM complex was calculated from the linear plot of $\sqrt{(-\log K_{av})}$ vs R_H as previously described (Laurent and Killander, 1964; Siegel and Monty, 1966)

Dynamic light scattering

The dynamic light scattering (DLS) experiments were performed with purified human Kir2.1 channel on a DynaPro instrument (Wyatt Technology Corp., Santa Barbara, CA). Measurements were carried out with 20 µL of Kir2.1 in TKED buffer at varying concentrations (0.1 – 0.8 mg·mL^{-1}). The sample temperature was set to 8 °C with TC100-830 Temperature Controlled MicroSampler (Protein Solutions/Wyatt Technology Corp). The laser light wavelength was 830 nm, the scattered light was collected at 90° of the incident light, and the correlation time was set to 0.5 ms with an acquisition time of 10 s for a total measurement of up to 1600 s. DLS data were analyzed using Dynamics software versions 6 and 7 (Wyatt Technology Corp.) to provide the R_H and the polydispersity percentage (%P, standard deviation).

SEC-MALLS-RI, a triple detection method to characterize membrane proteins in solution.

SEC-MALLS-RI experiments were carried out on a Shimadzu HPLC coupled to an Optilab T-rEX refractometer and a miniDawn TREOS Multi-Angle Laser Light Scattering (MALLS) detector (both from Wyatt Technology). A Superdex 200 Increase column (Cytiva), equivalent to the S200-GL column but supporting high pressure, was used. The system was equilibrated overnight with the SEC mobile phase (20 mM Tris-HCl, pH 7.4, 150 mM KCl, 1 mM EDTA, and 0.03% DDM) at 0.3 mL·min^{-1} flow rate. The RI purge was set in on-mode to equilibrate the reference and measurement chambers. The temperature of the refractometer cell was fixed at 25 °C. The next day, the UV lamp and LS laser were turned on. Once the UV, LS, and RI baselines were stable, the mobile phase RI was noted, the RI purge was switched off, and the RI baseline was set to zero. 20 µL of BSA at 5 mg·mL^{-1} were injected to calculate the inter-detector volumes. The signal-acquisition interval was set to 0.125 s. The molar mass of molecules (membrane protein detergent complexes and detergent micelles) passing through the SEC column could then be determined without calibration by measuring their static light scattering and knowing the respective extinction coefficients and refractive index increments of the protein and the detergent, by using the module Protein Conjugate from the Astra V software (Wyatt Technology). The methodology of mass calculation is thoroughly described in (Mégret-Cavalier et al., 2024) and detailed in the supplementary material.

Determination of the mass of the Kir2.1-DDM complex. First, Kir2.1 samples were analyzed following isolation of the estimated tetramer peak post-SEC purification, concentrated about 100 times with a 100 kDa cutoff filter. 20 µL of Kir2.1 at 0.8 mg·mL^{-1} in 0.03% DDM were injected and eluted at 0.4 mL·min^{-1} flow rate at room temperature. The best results were obtained when the protein was injected into SEC-MALLS just after affinity chromatography. The flow rate was reduced from 0.4 mL·min^{-1} to 0.3 mL·min^{-1} and the column was systematically washed with NaOH to remove background noise coming from impurities fixed on the column. The same protocol was used for all other detergent/protein Kir2.1 mixtures.

Surface plasmon resonance

The interaction between Kir2.1 and the lipid PIP_2 was characterized by SPR on a Biacore 3000 instrument (Cytiva) controlled by Biacore 3000 Control software v4.1. The

experiments were performed following the protocol described in (Fernandes and Zuniga et al., 2022). All biosensor experiments were performed in triplicate at 25 °C using the running buffer 20 mM Tris-HCl (pH 7.5), 150 mM KCl, 0.05 mM EDTA, and 0.05% DDM). Kir2.1-C154Y was immobilized onto a carboxymethylated dextran (CM5) sensor chip. The activation of CM5 chips and immobilization of the protein steps were done using standard Biacore procedures. The binding and kinetic assays were performed using single-cycle kinetics. PIP_2 was serially diluted in running buffer to working concentrations (1.25 µM to 20 µM). For each cycle, PIP_2 was injected at increasing concentration with a flow of 5 $\mu L \cdot min^{-1}$ over both the reference cell and the ligand cell. Each injection consisted of 300-s contact time with 300-s dissociation time. No regeneration step was done between Injections, as these buffers were detrimental to Kir2.1. The data were analyzed using BIA evaluation software 4.1, and kinetic parameters were determined using general fit and the titration kinetics 1:1 binding with drift model. The association and dissociation rate constants, k_{on} and k_{off}, respectively, and the K_D were determined directly from the fitted curves.

Sample preparation and cryo-EM data collection of Kir2.1-R312H mutant

Three microliters of Kir2.1 R312H mutant form were placed on glow-discharged (25 s) holey carbon-coated grids (Quantifoil R1.2/1.3, Au 200 mesh), blotted for 3.0 s, and flash-frozen in liquid ethane using a Vitrobot Mark III (Thermo Fisher Scientific) operated at 4 °C and 100% humidity. The EM data collection statistics are available in Table S2. A total of 10,762 movies were collected on a Titan Krios G4i microscope at Institut Pasteur (Paris) operated at 300 kV equipped with a Falcon 4 direct electron detector and a Selectrix Image Filter (Thermo Fisher Scientific). The automation of the data collection was done with the software EPU. Movies were recorded in electron-counting mode using EER fractionation at 165,000x nominal magnification with an exposure time of 2.93 s, and a total dose of 40 electrons/Å. A defocus range of −1.2 to −2.4 µm was used and two images were acquired per foil hole. The pixel size was 0.73 Å/pixel.

Cryo-EM data processing of Kir2.1-R312H mutant CTD domain

The movies were motion-corrected and dose-weighted using MotionCor2 (Zheng et al., 2017), and contrast function parameters (CTF) were estimated using CTFFIND4 (Rohou and Grigorieff, 2015). The corrected micrographs were filtered using a maximum CTF-fit resolution of 8 Å and a maximum total full-frame motion distance of 20 pixels. The image processing was then performed using CryoSPARC (Punjani et al., 2017). A blob picking followed by 2D classification was performed to generate templates for automated template-picking. Initially, 2,787,753 particles were selected after template-picking, which were submitted to three rounds of 2D classification to remove false picks, ice contamination, and classes with unclear features. A total of 146,539 particles were subjected to 3D *ab initio* reconstruction using no symmetry, followed by a single round of non-uniform refinement using C4 symmetry that provided a map of the entire protein at 6 Å resolution. Then, in order to focus on the CTD domain, where the R312H mutation is placed, and improve the resolution, a particle subtraction operation was performed to remove the TMD signal followed by a single round of local refinement of the CTD domain. The resolution of the final map of the CTD domain of Kir2.1 R312H mutant is

5.3 Å (gold-standard FSC= 0.143). Cryo-EM data collection information is summarized in Table S2.

Molecular dynamics simulations of Kir2.1 C154Y mutant

To evaluate the impact of C154Y mutation on the structure and dynamics of Kir2.1 channels, this mutation was modeled on the cryo-EM structure of the human Kir2.1 channel (PDB ID 7ZDZ) (Fernandes and Zuniga et al., 2022) using the CHARMM-GUI server (Jo et al., 2008), followed by MD simulations employing NAMD software (Phillips et al., 2005) under the CHARMM36m force field (Huang and MacKerell, 2013). For that, the mutation was placed in one monomer (Chain A_{C154Y}), in two adjacent (side-by-side) monomers (Chains AB_{C154Y}), in two diagonally opposite monomers (Chains AC_{C154Y}), in three monomers (Chains ABC_{C154Y}) and four monomers (Chains $ABCD_{C154Y}$) of the Kir2.1 tetramer. All preparation steps were performed using the CHARMM-GUI server (Jo et al., 2008). All mutant forms designed were embedded in a 100% POPC lipid bilayer and it was used a KCl concentration of 0.15 M was used to calculate the number of neutralizing atoms. The system was heated and equilibrated in the standard equilibration protocol suggested by CHARMM-GUI developers, gradually decreasing protein and membrane atomic positional restraints for 2 ns. Last, the production run was performed without any positional restraints for 200 ns (2000 frames; 0.1 ns per frame) in triplicate. The dihedral angles of the T142, I143 and Y145 residues were calculated using the command QUICK in CHARMM (Brooks et al., 1983) following the atom sequence available in the protein structure file (psf) obtained with the CHARMM-GUI: Cα, Cβ, Cγ, and C for T142; Cα, Cβ, Cδ, and C for I143; and Cα, Cβ, Cζ, and C for Y145. A similar protocol was used to perform three 200 ns-replica of MD simulations with the mutations C154S, C122Y/C154Y, and C122W/C154W placed on the four chains of the Kir2.1 structure. The rmsf and T142, I143, and Y145 dihedral angles were calculated as before.

H221R/R312H double-mutant modeling

The H221R/R312H double-mutant was modeled on the human Kir2.1 channel cryo-EM structure (PDB ID 7ZDZ) by replacing the R312 and H221 residues with the most likely rotamers of histidine and arginine, respectively, in the Chimera software. Next, local energy minimization was performed using Chimera (around 6.5 Å of the modeled histidine, keeping other protein atoms fixed) using 1000 steepest descent steps (0.02-Å step size), 20 conjugate gradient steps (0.02-Å step size), and the AMBER ff14SB force field. After energy minimization, no clashes and bad contacts were observed between the modeled histidine and arginine residues and their vicinity.

Accession numbers: PDB 8QQL and EMD-18595

Funding: This work was supported by AFM-Téléthon #23207 for C.V.-B., Ecole Doctorale ED515 Sorbonne Université for D.Z., and EQUIPEX CACSICE ANR-11-EQPX-0008 (C.V.-B.). C.A.H.F. has received funding from the European Union's Horizon Europe Research and Innovation Program under grant agreement no. 101026386.

Acknowledgments

We thank C. Travert and Dr. F. Skouri-Panet for GEMME biochemistry & geobiology facility at IMPMC; Dr. S. Finet at IMPMC for training in use of DLS equipment and analysis; R. Boucher for his help on MD simulation; Nanoimaging Core facility (C2RT) at the Institut Pasteur and the help of J.-M. Winter, E. Salazar, S. Tachon, and M. Vos.

References

Bannister JPA, Young BA, Sivaprasadarao A, Wray D. 1999. Conserved extracellular cysteine residues in the inwardly rectifying potassium channel Kir2.3 are required for function but not expression in the membrane. *Febs Lett* **458**:393–399. doi:10.1016/S0014-5793(99)01096-0

Bendahhou S, Fournier E, Sternberg D, Bassez G, Furby A, Sereni C, Donaldson MR, Larroque MM, Fontaine B, Barhanin J. 2005. In vivo and in vitro functional characterization of Andersen's syndrome mutations. *J Physiol* **565**:731–41. doi:10.1113/jphysiol.2004.081620

Bergendahl LT, Gerasimavicius L, Miles J, Macdonald L, Wells JN, Welburn JPI, Marsh JA. 2019. The role of protein complexes in human genetic disease. *Protein Sci Publ Protein Soc* **28**:1400–1411. doi:10.1002/pro.3667

Brooks B, Bruccoleri R, Olafson B, States D, Swaminathan S, karplus M. 1983. CHARMM - A program for macromolecular energy, minimization, and dynamics calculations. *J Comput Chem* **4**:187–217. doi:10.1002/jcc.540040211

Cho HC, Tsushima RG, Nguyen TTT, Guy HR, Backx PH. 2000. Two critical cysteine residues implicated in disulfide bond formation and proper folding of Kir2.1. *Biochemistry* **39**:4649–4657. doi:10.1021/bi992469g

Coyote-Maestas W, Nedrud D, He Y, Schmidt D. 2022. Determinants of trafficking, conduction, and disease within a K+ channel revealed through multiparametric deep mutational scanning. *Elife* **11**:e76903. doi:10.7554/eLife.76903

D'Avanzo N, Cheng WWL, Doyle DA, Nichols CG. 2010a. Direct and Specific Activation of Human Inward Rectifier K+ Channels by Membrane Phosphatidylinositol 4,5-Bisphosphate. *J Biol Chem* **285**:37129–37132. doi:10.1074/jbc.C110.186692

D'Avanzo N, Cheng WWL, Xia X, Dong L, Savitsky P, Nichols CG, Doyle DA. 2010b. Expression and purification of recombinant human inward rectifier K+ (KCNJ) channels in Saccharomyces cerevisiae. *Protein Expr Purificatoon* **71**:115–121. doi:10.1016/j.pep.2010.01.010

Despa F, Orgill DP, Lee RC. 2005. Molecular crowding effects on protein stability. *Ann N Y Acad Sci* **1066**:54–66. doi:10.1196/annals.1363.005

Deutsch C. 2002. Potassium channel ontogeny. *Annu Rev Physiol* **64**:19–46. doi:10.1146/annurev.physiol.64.081501.155934

Doupnik CA, Davidson N, Lester HA. 1995. The inward rectifier potassium channel family. *Curr Opin Neurobiol* **5**:268–77.

Doyle DA, Cabral JM, Pfuetzner RA, Kuo AL, Gulbis JM, Cohen SL, Chait BT, MacKinnon R. 1998. The structure of the potassium channel: Molecular basis of K+ conduction and selectivity. *Science* **280**:69–77.

Fernandes CAH, Zuniga D, Fagnen C, Kugler V, Scala R, Péhau-Arnaudet G, Wagner R, Perahia D, Bendahhou S, Vénien-Bryan C. 2022. Cryo-electron microscopy unveils unique structural features of the human Kir2.1 channel. *Sci Adv* **8**:eabq8489. doi:10.1126/sciadv.abq8489

Gerasimavicius L, Livesey BJ, Marsh JA. 2022. Loss-of-function, gain-of-function and dominant-negative mutations have profoundly different effects on protein structure. *Nat Commun* **13**:3895. doi:10.1038/s41467-022-31686-6

Hager NA, McAtee CK, Lesko MA, O'Donnell AF. 2021. Inwardly Rectifying Potassium Channel Kir2.1 and its "Kir-ious" Regulation by Protein Trafficking and Roles in Development and Disease. *Front Cell Dev Biol* **9**:796136. doi:10.3389/fcell.2021.796136

Hansen SB, Tao X, MacKinnon R. 2011. Structural basis of PIP2 activation of the classical inward rectifier K+ channel Kir2.2. *Nature* **477**:495-U152. doi:10.1038/nature10370

Hartmann L, Kugler V, Wagner R. 2016. Expression of Eukaryotic Membrane Proteins in Pichia pastoris In: MusVeteau I, editor. Heterologous Expression of Membrane Proteins: Methods and Protocols, 2nd Edition. Totowa: Humana Press Inc. pp. 143–162. doi:10.1007/978-1-4939-3637-3_10

Hattori T, Makiyama T, Akao M, Ehara E, Ohno S, Iguchi M, Nishio Y, Sasaki K, Itoh H, Yokode M, Kita T, Horie M, Kimura T. 2012. A novel gain-of-function KCNJ2 mutation associated with short-QT syndrome impairs inward rectification of Kir2.1 currents. *Cardiovasc Res* **93**:666–673. doi:10.1093/cvr/cvr329

Hibino H, Inanobe A, Furutani K, Murakami S, Findlay I, Kurachi Y. 2010. Inwardly Rectifying Potassium Channels: Their Structure, Function, and Physiological Roles. *Physiol Rev* **90**:291–366. doi:10.1152/physrev.00021.2009

Huang J, MacKerell AD Jr. 2013. CHARMM36 all-atom additive protein force field: Validation based on comparison to NMR data. *Joiurnal Comput Chem* **34**:2135–2145. doi:10.1002/jcc.23354

Jo S, Kim T, Iyer VG, Im W. 2008. Software news and updates - CHARNIM-GUI: A web-based grraphical user interface for CHARMM. *J Comput Chem* **29**:1859–1865. doi:10.1002/jcc.20945

Katz B. 1949. Les constantes électriques de la membrane du muscle. *Arch Sci Physiol (Paris)* **3**:285–300.

Laurent T, Killander J. 1964. Theory of gel filtration - Its experimental verification. *J Chromatogr*. doi:10.1016/S0021-9673(00)86637-6

Levesque I, Juliano BR, Parson KF, Ruotolo BT. 2023. A Critical Evaluation of Detergent Exchange Methodologies for Membrane Protein Native Mass Spectrometry. *J Am Soc Mass Spectrom* **34**:2662–2671. doi:10.1021/jasms.3c00230

Leyland ML, Dart C, Spencer PJ, Sutcliffe MJ, Stanfield PR. 1999. The possible role of a disulphide bond in forming functional Kir2.1 potassium channels. *Pflugers Arch-Eur J Physiol* **438**:778–781. doi:10.1007/s004240051106

Mégret-Cavalier M, Pozza A, Cece Q, Bonneté F, Broutin I, Phan G. 2024. Starting with an Integral Membrane Protein Project for Structural Biology: Production, Purification, Detergent Quantification, and Buffer Optimization-Case Study of the Exporter CntI from Pseudomonas aeruginosa. *Methods Mol Biol Clifton NJ* **2715**:415–430. doi:10.1007/978-1-0716-3445-5_26

Missel JW, Salustros N, Becares ER, Steffen JH, Laursen AG, Garcia AS, Garcia-Alai MM, Kolar Č, Gourdon P, Gotfryd K. 2021. Cyclohexyl-α maltoside as a highly efficient tool for membrane protein studies. *Curr Res Struct Biol* **3**:85–94. doi:10.1016/j.crstbi.2021.03.002

Nguyen H-L, Pieper GH, Wilders R. 2013. Andersen-Tawil syndrome: clinical and molecular aspects. *Int J Cardiol* **170**:1–16. doi:10.1016/j.ijcard.2013.10.010

Phillips J, Braun R, Wang W, Gumbart J, Tajkhorshid E, Villa E, Chipot C, Skeel R, Kale L, Schulten K. 2005. Scalable molecular dynamics with NAMD. *J Comput Chem* **26**:1781–1802. doi:10.1002/jcc.20289

Plaster NM, Tawil R, Tristani-Firouzi M, Canun S, Bendahhou S, Tsunoda A, Donaldson MR, Iannaccone ST, Brunt E, Barohn R, Clark J, Deymeer F, George AL Jr, Fish FA, Hahn A, Nitu A, Ozdemir C, Serdaroglu P, Subramony SH, Wolfe G, Fu YH, Ptacek LJ. 2001. Mutations in Kir2.1 cause the developmental and episodic electrical phenotypes of Andersen's syndrome. *Cell* **105**:511–9.

Punjani A, Rubinstein JL, Fleet DJ, Brubaker MA. 2017. cryoSPARC: algorithms for rapid unsupervised cryo-EM structure determination. *Nat Methods* **14**:290–296. doi:10.1038/nmeth.4169

Reilly L, Eckhardt LL. 2021. Cardiac potassium inward rectifier Kir2: Review of structure, regulation, pharmacology, and arrhythmogenesis. *Heart Rhythm* **18**:1423–1434. doi:10.1016/j.hrthm.2021.04.008

Rohou A, Grigorieff N. 2015. CTFFIND4: Fast and accurate defocus estimation from electron micrographs. *J Struct Biol* **192**:216–221. doi:10.1016/j.jsb.2015.08.008

Sacconi S, Simkin D, Arrighi N, Chapon F, Larroque MM, Vicart S, Sternberg D, Fontaine B, Barhanin J, Desnuelle C, Bendahhou S. 2009. Mechanisms underlying Andersen's syndrome pathology in skeletal muscle are revealed in human myotubes. *Am J Physiol Cell Physiol* **297**:C876-85. doi:10.1152/ajpcell.00519.2008

Siegel LM, Monty KJ. 1966. Determination of molecular weights and frictional ratios of proteins in impure systems by use of gel filtration and density gradient centrifugation. Application to crude preparations of sulfite and hydroxylamine reductases. *Biochim Biophys Acta* **112**:346–362. doi:10.1016/0926-6585(66)90333-5

Strop P, Brunger AT. 2005. Refractive index-based determination of detergent concentration and its application to the study of membrane proteins. *Protein Sci Publ Protein Soc* **14**:2207–2211. doi:10.1110/ps.051543805

Tao X, Avalos JL, Chen JY, MacKinnon R. 2009. Crystal Structure of the Eukaryotic Strong Inward-Rectifier K+ Channel Kir2.2 at 3.1 angstrom Resolution. *Science* **326**:1668–1674. doi:10.1126/science.1180310

Valiyaveetil FI, Sekedat M, Mackinnon R, Muir TW. 2004. Glycine as a D-amino acid surrogate in the K(+)-selectivity filter. *Proc Natl Acad Sci U S A* **101**:17045–17049. doi:10.1073/pnas.0407820101

Xia M, Jin Q, Bendahhou S, He Y, Larroque MM, Chen Y, Zhou Q, Yang Y, Liu Y, Liu B, Zhu Q, Zhou Y, Lin J, Liang B, Li L, Dong X, Pan Z, Wang R, Wan H, Qiu W, Xu W, Eurlings P, Barhanin J. 2005. A Kir2.1 gain-of-function mutation underlies familial atrial fibrillation. *Biochem Biophys Res Commun* **332**:1012–9. doi:10.1016/j.bbrc.2005.05.054

Xue T, Marbán E, Li RA. 2002. Dominant-negative suppression of HCN1- and HCN2-encoded pacemaker currents by an engineered HCN1 construct: insights into structure-function relationships and multimerization. *Circ Res* **90**:1267–1273. doi:10.1161/01.res.0000024390.97889.c6

Zheng SQ, Palovcak E, Armache J-P, Verba KA, Cheng Y, Agard DA. 2017. MotionCor2: anisotropic correction of beam-induced motion for improved cryo-electron microscopy. *Nat Methods* **14**:331–332. doi:10.1038/nmeth.4193

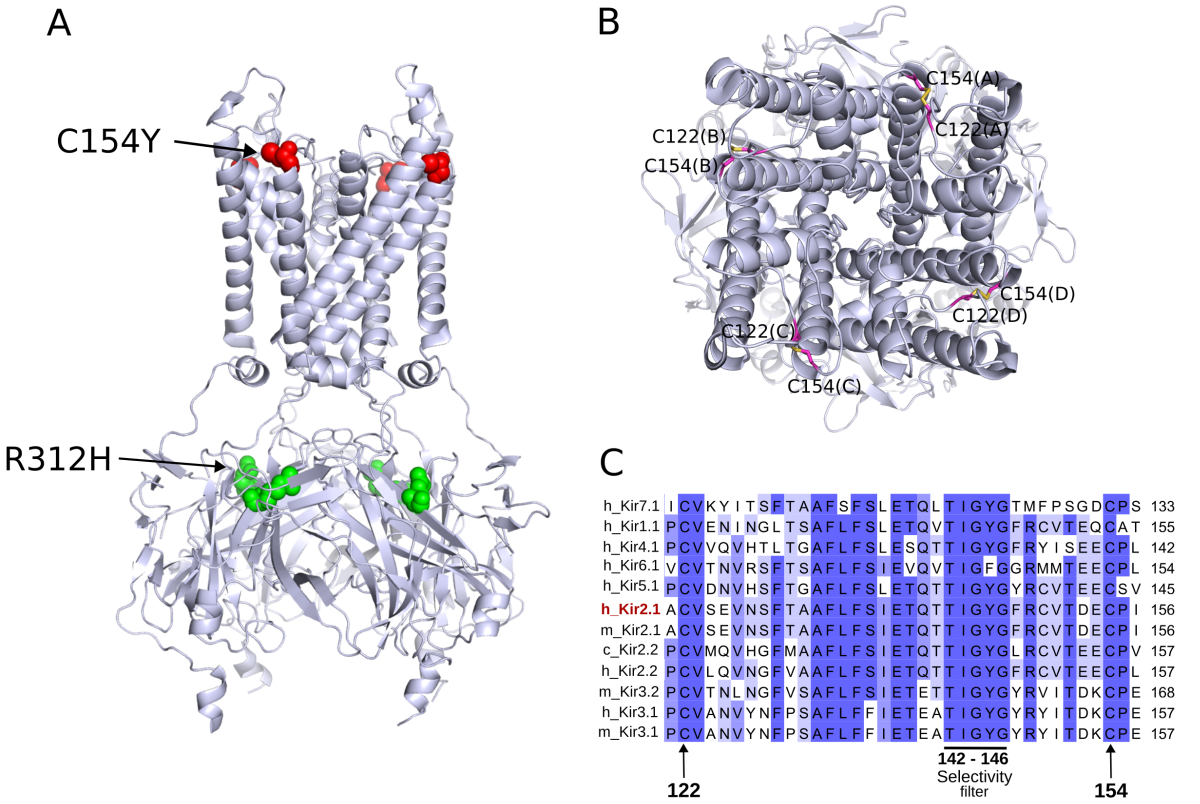

Figure 1. Location of C154Y and R312H mutations associated with Andersen-Tawil syndrome on human Kir2.1 channel and their effects on the channel current. A. Cartoon representation of the cryo-EM structure of the human Kir2.1 channel (PDB ID 7ZDZ) where the location of the C154Y and R312H mutations is highlighted on the channel structure (red and green spheres, respectively). **B**. Top view of the human Kir2.1 channel structure where the intra-subunit disulfide bond formed by C122 and C154 is highlighted in magenta sticks. The chains are indicated in parentheses. **C**. Amino acid sequence alignment of the region comprising residues 121 to 155 (Kir2.1 numbering) between different Kir channels. The conserved C122 and C154 residues are indicated by black arrows (numbers 122 and 154). The alignment also highlights the selectivity filter of the Kir channels (residues 142- 146). The highly conserved amino acids are highlighted in purple. h_Kir: Human Kir, m_Kir: mouse Kir, c_Kir: chicken Kir. The amino acid sequence of the human Kir2.1 channel (h_Kir2.1) is highlighted in red.

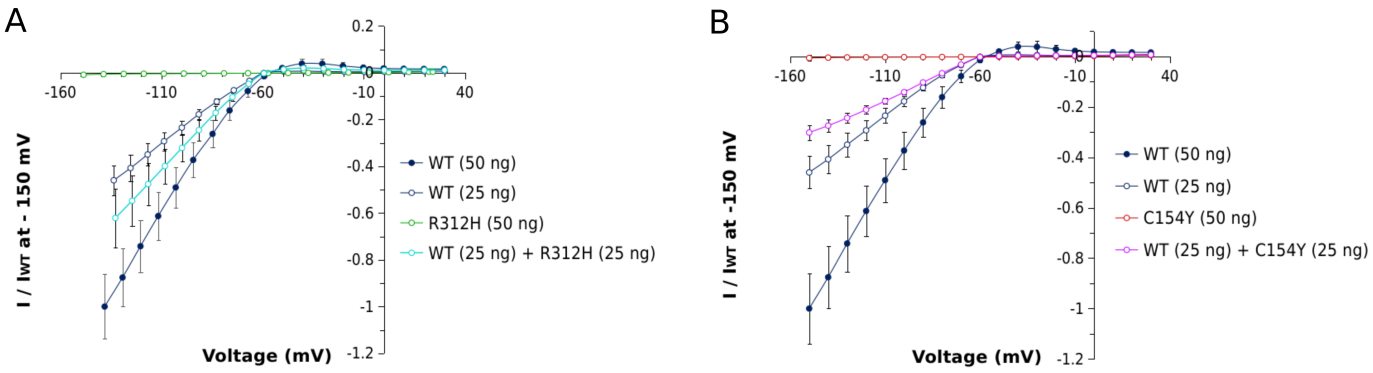

Figure 2. Functional expression of Kir2.1-WT and C154Y and R312H mutants in *Xenopus laevis* oocytes. Normalized current-voltage (I-V) relationships of the macroscopic currents of the Kir2.1 WT alone (injections of 50 ng and 25 ng of WT cDNA, blue and gray curves, respectively) and (**A**) R312H mutant alone (50 ng of R312H cDNA, green curve) or co-injected with WT cDNA (25 ng of WT cDNA + 25 ng of R312H cDNA, cyan curve), and (**B**) C154Y mutant alone (50 ng of C154Y cDNA, red curve) or co-injected with WT cDNA (25 ng of WT cDNA + 25 ng of C154Y cDNA, purple curve) compared to the control current of Kir2.1-WT (50 ng and 25 ng of cDNA, blue and gray curves) at −150 mV. Currents were elicited by 500 ms pulses from −150 mV to +30 mV in 10 mV increments from a holding potential of −60 mV. Values were measured at the end of each step pulse and represent mean ± SEM, n = 5-9 oocytes per group.

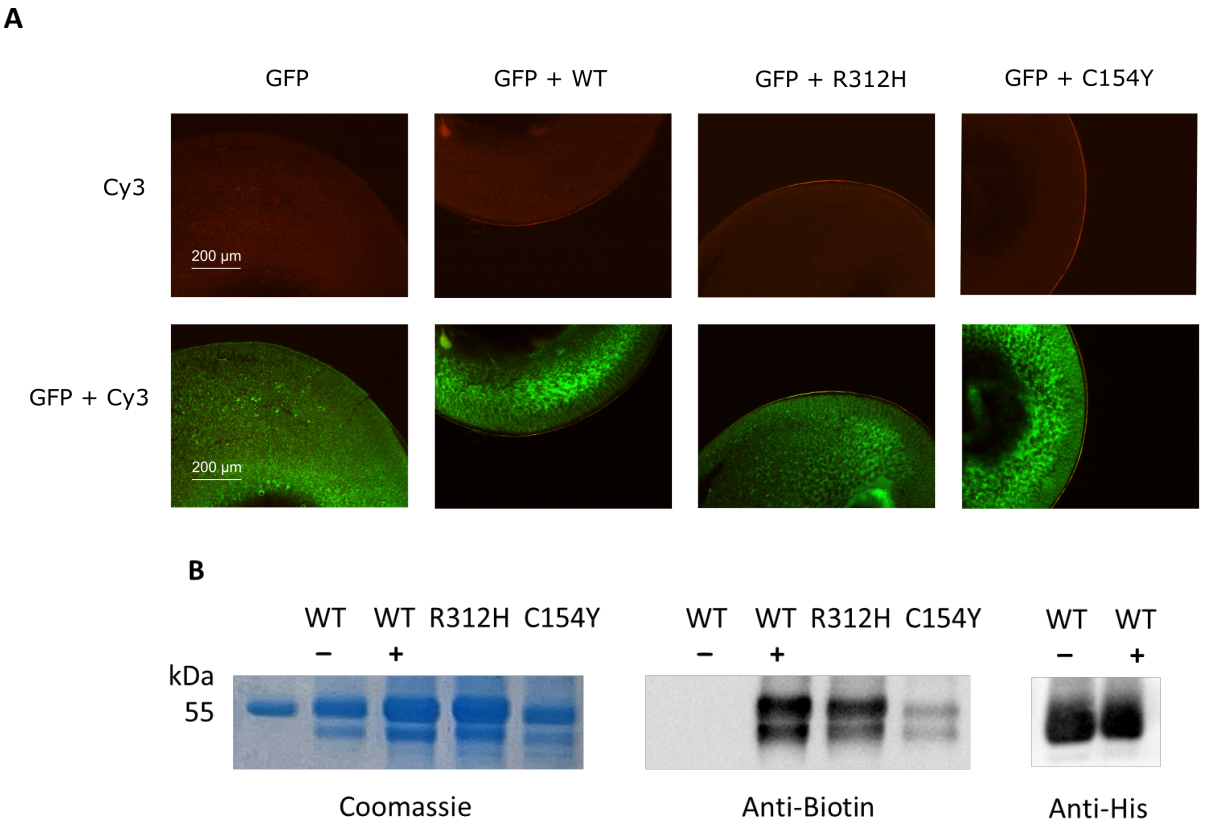

Figure 3. Trafficking of the Kir2.1-WT and R312H and C154Y mutants to the membrane. **A.** Immunofluorescence assays conducted in *Xenopus laevis* oocytes expressing Kir2.1-WT and mutants. Top row: visualization of Cy3-conjugated anti-rabbit secondary antibody (the primary antibody is a rabbit anti-Kir2.1) showing the location of Kir2.1-WT, Kir2.1-R312H, and Kir2.1-C154Y in the membrane (orange). Control (no cDNA Kir2.1 injected) is shown top left. Bottom row: same as top row but with the co-visualization of the co-injected green fluorescent protein (GFP), which is used to confirm the successful injection of cDNA into the oocytes. Oocytes were co-injected with 50 ng of cDNA encoding Kir2.1 (WT, R312H or C154Y) and 25 ng of cDNA encoding GFP or injected only with 25 ng of cDNA encoding GFP when indicated. Three independent experiments in three different oocytes batches were performed, and the results were consistently similar. One representative experiment is shown in the figure. **B.** Cell surface protein biotinylation assays in *Pichia pastoris* cells. Left: SDS-PAGE of Kir2.1-WT and mutants purified after biotinylation and affinity chromatography revealed by Coomassie blue. Middle: Western blot and Extravidin-HRP reaction highlighting the presence of protein Kir2.1-WT, and R312H and C154Y mutants at the membrane level. WT (-) is the result with the non-biotinylated membrane. Right: Western-blot revealed by Anti-His antibody interaction with His-tagged Kir2.1.

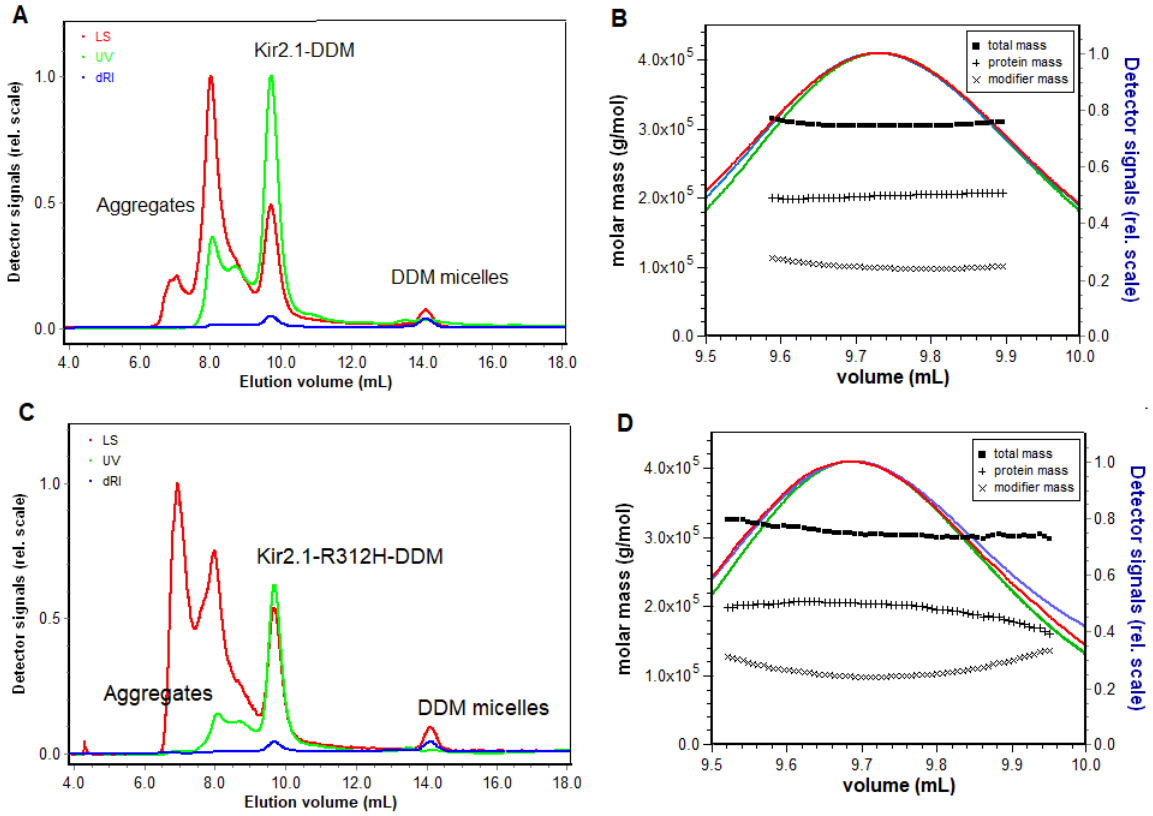

Figure 4. Biophysical characterization of the quaternary structure of Kir2.1-WT and R312H mutant. A. SEC-MALLS-RI profile of Kir2.1-WT in 20 mM Tris-HCl pH 7.4, 150 mM KCl, 1 mM EDTA, 0.03% DDM (eluted on Superdex10/300 200 Increase); **B.** Zoom on the peak corresponding to Kir2.1 tetramers; **C.** SEC-MALLS-RI profile of Kir2.1-R312H in 20 mM Tris-HCl pH 7.4, 150 mM KCl, 1 mM EDTA, 0.03% DDM; **D.** Zoom on the peak corresponding to Kir2.1-R312H tetramers. On each figure, the LS, UV, and RI profiles are shown in red, green, and blue respectively. Molar mass distribution vs elution volume of Kir2.1-DDM and Kir2.1-R312H-DDM complex were calculated using the module Protein Conjugate from the Astra V software (Wyatt Technology). A perfect alignment of the 3 signals (LS, UV, and RI) is observed at the center of the peaks. The total complex mass Kir2.1 molar mass, and DDM molar mass are shown as horizontal lines across the peak, depicting a monodisperse complex in DDM for both Kir2.1-WT and Kir2.1-R312H.

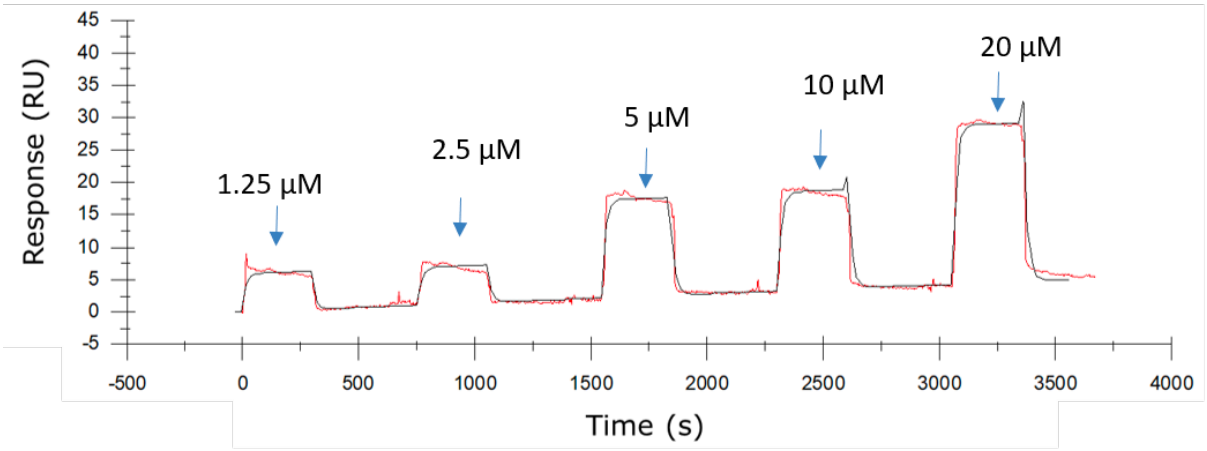

Figure 5. Surface plasmon resonance (SPR) sensorgram of the Kir2.1-C154Y mutant (5844 RU level) immobilized onto a CM5 chip. Five sequential injections of PIP_2 are shown, at 1.25-20 µM, and a flow of 5 $\mu L \cdot min^{-1}$. In color, experimental data; in black, the fitted curve. The sensorgram is expressed in response units (RU) relative to the time in seconds.

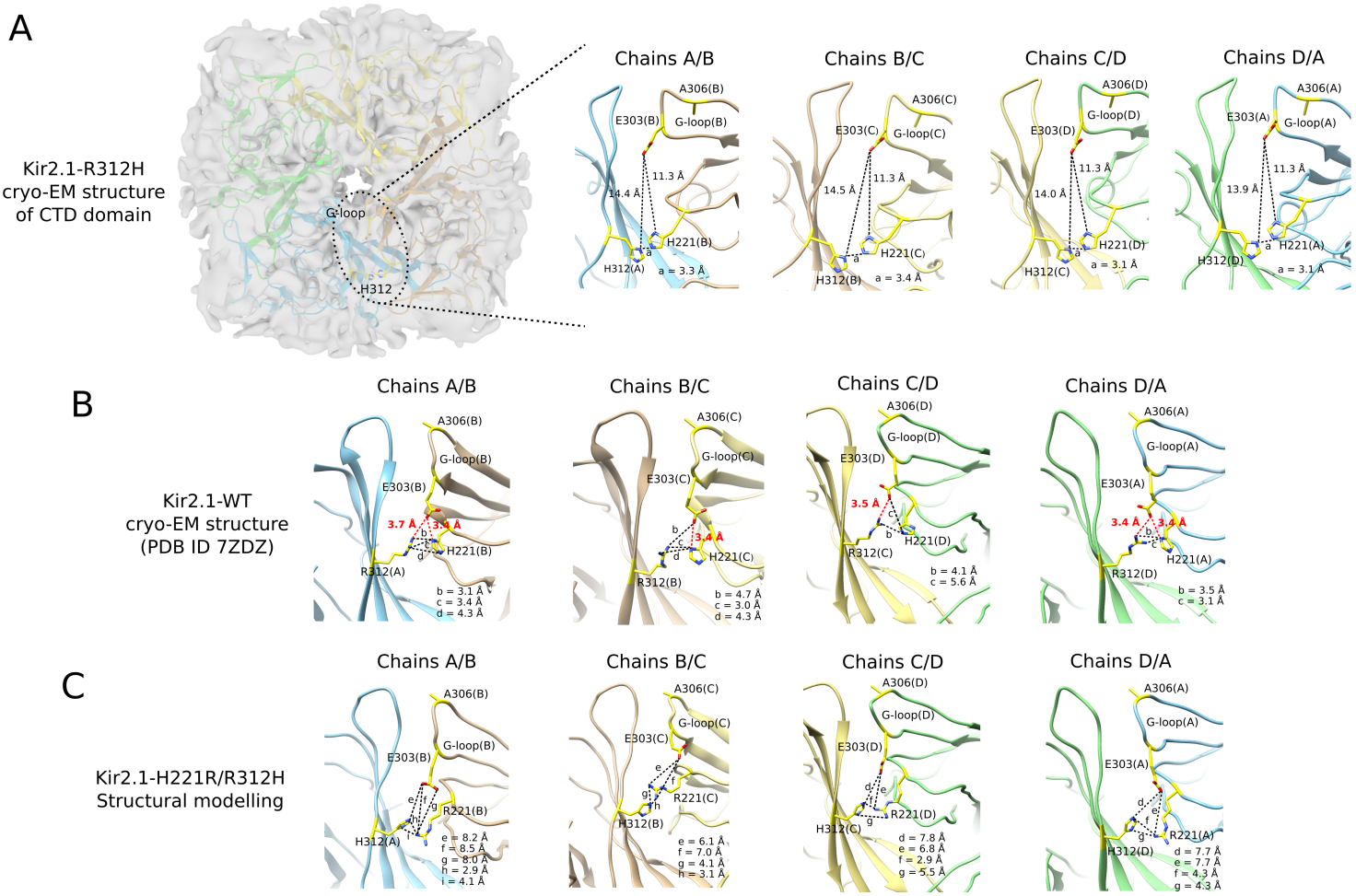

Figure 6. Cryo-EM structure of the cytoplasmic domain (CTD) of Kir2.1-R312H mutant and structural impact of the R312H mutation in the human Kir2.1 channel. A. Top view of the sharpened cryo-EM map (gray surface) and atomic structure (in cartoon) of the CTD of the Kir2.1-R312H mutant. The circle highlights the location of the H312 residue and the insets show the distances of H312 from the four chains with the H221 and E303 residues from the clockwise-adjacent chain. **B.** Inter-subunit interaction network formed by R312 residue from the four chains with H221 and E303 residues from the clockwise-adjacent chain in the cryo-EM structure of Kir2.1-WT (PDB 7ZDZ). **C.** Distances between H312 residue from the four chains with R221 and E303 residues from the structural model of Kir2.1-H221R/R312H double-mutant obtained after molecular modeling. The chains A, B, C, and D are shown in blue, light brown, yellow, and green, respectively. Residues H221, R221, E303, A306, H312, and R312 are represented as yellow sticks. The chains are indicated in parentheses. Salt bridge distances are highlighted in red dashes and the other distances are highlighted in black dashes.

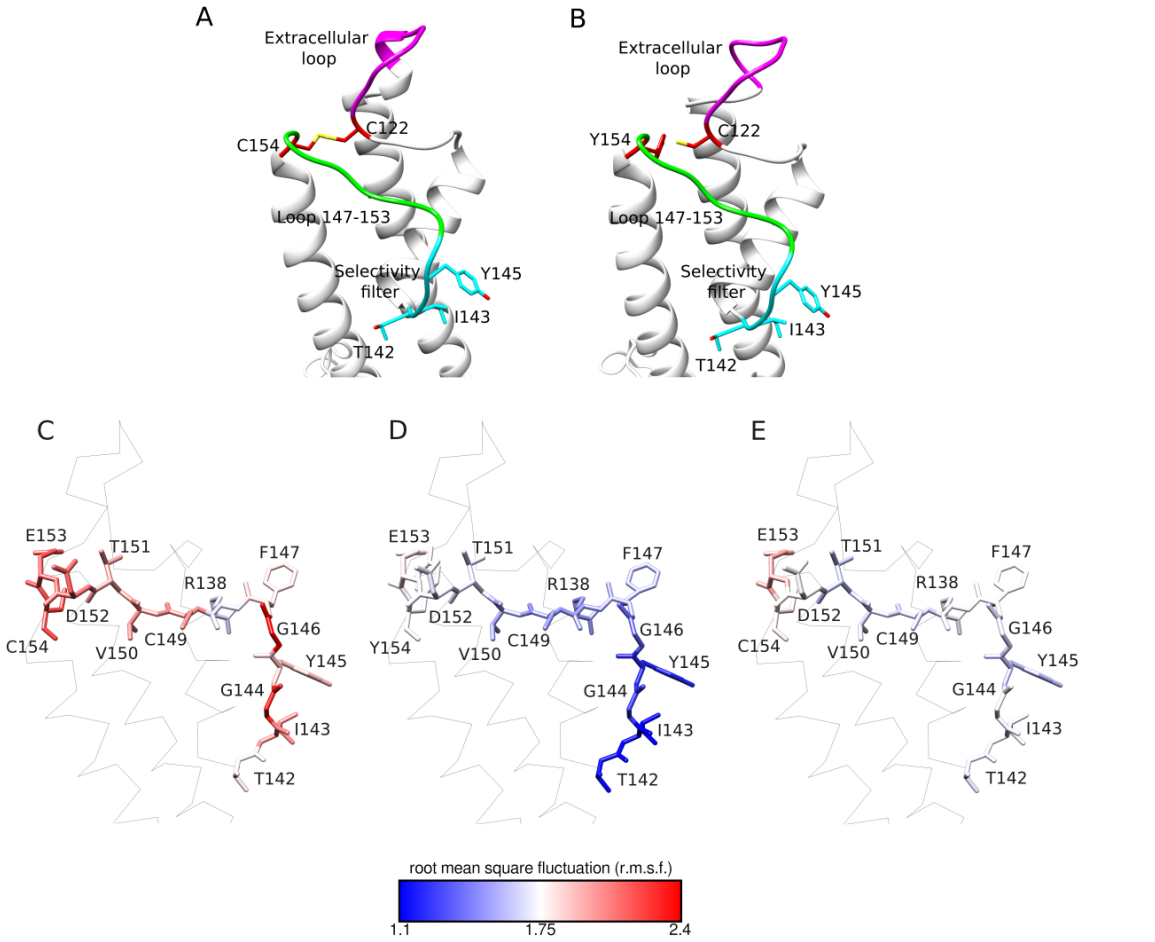

Figure 7. Analysis of the impact caused by the mutation C154Y on the Kir2.1 structure and on the root mean square fluctuation (rmsf) of the selectivity filter (region 142-146), the 147-153 loop, and the residue located at position 154. A. Kir2.1WT **B.** Kir2.1-C154Y Cartoon representation of the C122/C154 disulfide bond or C154Y and C122 are in red sticks. The extracellular loop (magenta) and the selectivity filter (cyan) are connected through the 146-153 loop (green). The residues T142, I143, and Y145 from the selectivity filter are highlighted in cyan sticks. **C.** A representative WT chain (C154) from a representative replica of MD simulations performed with the Kir2.1-WT cryo-EM structure (PDB ID 7ZDZ). **D.** A representative C154Y chain from a representative replica of MD simulations performed after incorporating the C154Y in the four subunits of the Kir2.1 tetramer. **E.** A representative WT chain (C154) from a representative replica of MD simulations performed with structures containing the assembly of both WT and C154Y mutated subunits in the Kir2.1 tetramer (hybrid WT-C154Y models). In panels C, D, and E, the backbone a segment of the Kir2.1 structure containing part of the transmembrane domain (TMD) and the extracellular loop is shown in gray. The residues on which the rmsf was evaluated are showed in sticks and labelled according to their names and position. These residues are colored based on their rmsf values which are represented on the color scale ranging from 1.1 (blue, less flexible) to 2.4 (red, more flexible).

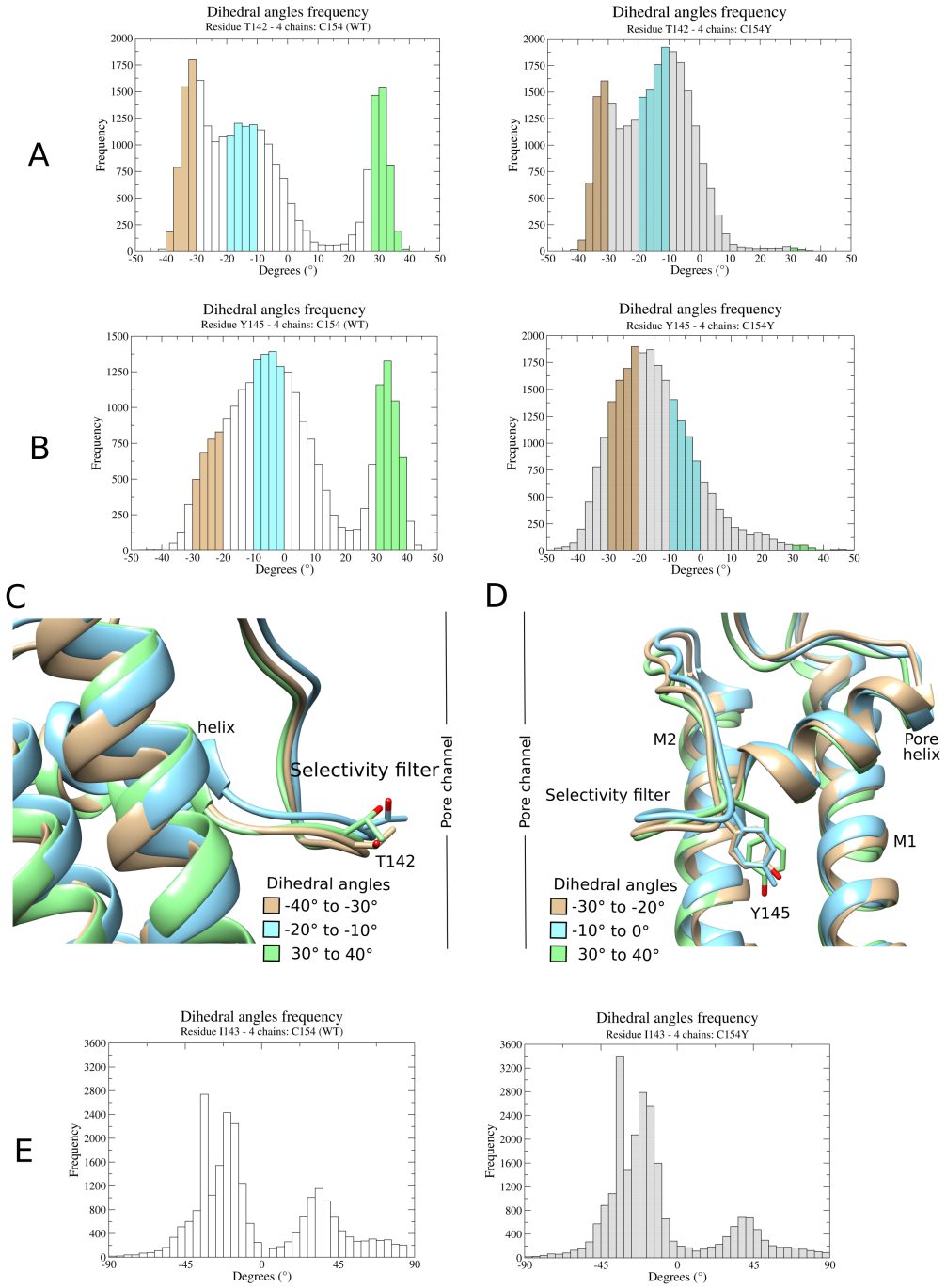

Figure 8. Dihedral angles analysis of the selectivity filter residues (T142, I143, and Y145) of the Kir2.1 channel. Dihedral angle frequency for the T142 (**panel A**), Y145 (**panel B**), and I143 (**panel E**) residues obtained along the 200 ns of MD simulations in triplicate of the Kir2.1 channel cryo-EM structure WT (four chains C154; left column) and after incorporating the C154Y mutation in the four subunits of the tetramer (Chains $ABCD_{C154Y}$; right column). For residue T142 (**panel A**), the frequency of dihedral angles in the ranges of −40° to −30°, −20° to −10°, and 30° to 40° are highlighted in brown, cyan, and green, respectively. For residue Y145 (**panel B**), the frequency of dihedral angles in the ranges of −30° to −20°, −10° to 0°, and 30° to 40° are highlighted in brown, cyan, and green, respectively. **Panels C and D** show snapshots captured along the MD simulations to illustrate these dihedral angle ranges for the side chains (shown in sticks) of the residues T142 (**panel C**) and Y145 (**panel D**). The dihedral angle

frequency analysis of residue I143 (**panel E**) is not highlighted because the impact of the C154Y mutation on it was inconclusive.

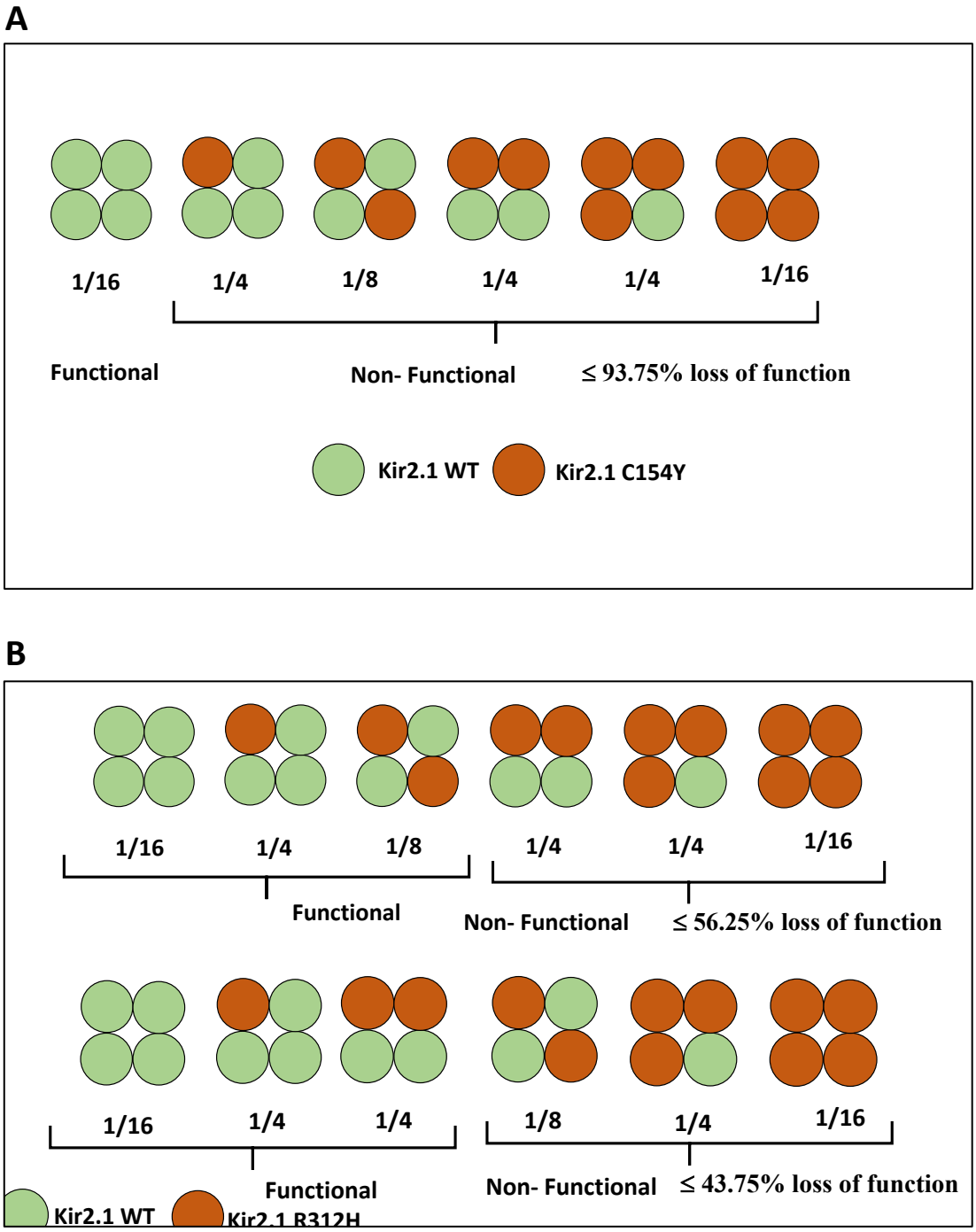

Figure 9. Probabilistic models of the effect of association between WT and mutant subunits in Kir2.1 tetrameric complexes. **A.** Model of the association between C154Y with WT subunits. This model predicts a dominant-negative effect of the C154Y mutation. One single C154Y mutant subunit blocks the activity of the entire complex, resulting in a loss-of-function of ≤ 93.75%. **B.** Model of the association between R312H and WT subunits. Two different propositions are presented in the upper and lower panels, respectively. The upper panel predicts a theoretical loss of function of ≤ 56.25% when R312H mutant subunits are placed side-by-side with WT subunits in the Kir2.1 tetramer. The lower panel predicts a theoretical loss of function of ≤ 43.75% when the R312H mutant subunits are placed diagonally opposed to WT subunits in the Kir2.1. These models were derived from a previously proposed probabilistic model (Bergendahl et al., 2019).

	Kir2.1 Chains A/B/C/D: C154 (WT)	**Kir2.1 Chains A/B/C/D: C154Y**	**Kir2.1 Chains A/B/C: C154Y Chain D: C154 (WT)**	**Kir2.1 Chains A/B: C154Y Chains C/D: C154 (WT)**	**Kir2.1 Chains A/C: C154Y Chains B/D: C154 (WT)**	**Kir2.1 Chain A: C154Y Chains A/B/D: C154 (WT)**
Position 154	Chains A/B/C/D_{WT}= 2.22±0.14	Chains A/B/C/D_{C154Y}= 1.74±0.17	Chains A/B/C_{C154Y}= 1.80±0.18 Chain D_{WT}= 2.02±0.11	Chains A/B_{C154Y}= 1.82±0.12 Chains C/D_{WT}= 2.20±0.18	Chains A/C_{C154Y}= 1.80 ±0.13 Chains B/D_{WT}= 2.16±0.18	Chain A_{C154Y}= 1.85±0.19 Chains B/C/D_{WT}=2.19±0.21
Loop 147-153	Chains A/B/C/D_{WT}= 2.01±0.12	Chains A/B/C/D_{C154Y}= 1.63±0.13	Chains A/B/C_{C154Y}=1.68±0.20 Chain D_{WT}=1.72±0.12	Chains A/B_{C154Y}= 1.75 ±0.14 Chains C/D_{WT}= 1.79±0.18	Chains A/C_{C154Y}= 1.70 ±0.16 Chains B/D_{WT}= 1.75±0.19	Chain A_{C154Y}= 1.79±0.11 Chains B/C/D_{WT}= 1.91±0.22
Selectivity filter (142-146)	Chains A/B/C/D_{WT}= 2.02±0.18	Chains A/B/C/D_{C154Y}= 1.23±0.05	Chains A/B/C_{C154Y}= 1.26±0.06 Chain D_{WT}= 1.59±0.12	Chains A/B_{C154Y}= 1.46±0.09 Chains C/D_{WT}= 1.65±0.11	Chains A/C_{C154Y}= 1.42±0.07 Chains B/D_{WT}= 1.62±0.13	Chain A_{C154Y}= 1.51±0.09 Chains B/C/D_{WT}= 1.79±0.17

Table 1. Average values of root mean square fluctuation (rmsf) calculated along the 200 ns of MD simulations in triplicate of the Kir2.1 channel cryo-EM structure WT (four chains C154) and after incorporating the C154Y mutation in the four subunits of the tetramer (Chains $ABCD_{C154Y}$), in three subunits (Chains ABC_{C154Y}, Chain D_{WT}), in two adjacent (side-by-side) subunits (Chains AB_{C154Y}, Chains CD_{WT}), in two diagonally opposite subunits (Chains AC_{C154Y}, Chains BD_{WT}), and in one subunit (Chain A_{C154Y}, Chains BCD_{WT}).

	Kir2.1 Chains A/B/C/D: C154 (WT)	Kir2.1 Chains A/B/C/D: C154Y	Kir2.1 Chains A/B/C: C154Y Chain D: C154 (WT)	Kir2.1 Chains A/B: C154Y ChainsC/D: C154 (WT)	Kir2.1 Chains A/C: C154Y Chains B/D: C154 (WT)	Kir2.1 Chain A: C154Y Chains A/B/D: C154 (WT)
T142	Chains $A/B/C/D_{WT}$= 16.1%	Chains $A/B/C/D_{C154Y}$= 0.3%	Chains $A/B/C_{C154Y}$=3.4% Chain D_{WT}=0.3%	Chains A/B_{C154Y}=0.2% Chains C/D_{WT}= 1.0%	Chains A/C_{C154Y}= 2.4% Chains B/D_{WT}= 6.8%	Chain A_{C154Y}=0.1% Chains $B/C/D_{WT}$=9.8%
I143	Chains $A/B/C/D_{WT}$= 12.9%	Chains $A/B/C/D_{C154Y}$= 6.1%	Chains $A/B/C_{C154Y}$= 8.7% Chain D_{WT}= 7.7 %	Chains A/B_{C154Y}= 20.0% Chains C/D_{WT}= 6.8 %	Chains A/C_{C154Y}= 6.3% Chains B/D_{WT}= 13%	Chain A_{C154Y}= 11.9% Chains $B/C/D_{WT}$= 4.0%
Y145	Chains $A/B/C/D_{WT}$= 18.2%	Chains $A/B/C/D_{C154Y}$= 0.8%	Chains $A/B/C_{C154Y}$= 3.2% Chain D_{WT}= 0.6%	Chains A/B_{C154Y}= 0.1% Chains C/D_{WT}= 1.1%	Chains A/C_{C154Y}= 0.2% Chains B/D_{WT}= 12.4%	Chain A_{C154Y}= 0.1% Chains $B/C/D_{WT}$= 10.3%

Table 2. Frequency of dihedral angles in the range of 30°—40° for the T142, I143, and Y145 residues. These values were obtained along the 200 ns of MD simulations in triplicate of the Kir2.1 channel cryo-EM structure WT (four chains C154) and after incorporating the C154Y mutation in the four subunits of the tetramer (Chains $ABCD_{C154Y}$), in three subunits (Chains ABC_{C154Y}, Chain D_{WT}), in two adjacent (side-by-side) subunits (Chains AB_{C154Y}, Chains CD_{WT}), in two diagonally opposite subunits (Chains AC_{C154Y}, Chains BD_{WT}), and in one subunit (Chain A_{C154Y}, Chains BCD_{WT}).